POLITECNICO DI TORINO

Master Degree course in Aerospace Engineering

Effects of leading edge tubercles on drone propeller performance

In collaboration with:

KTH Royal Institute of Technology

Supervised by:
Prof. Raffaello Mariani
Prof. Francesco Avallone
Eng. Alessandro Grava

Candidate:
Simone Basile

Academic Year 2023-2024

Ringraziamenti

In questi 8 anni di studio ho avuto modo di stringere e consolidare rapporti con persone che, in un modo o nell'altro, hanno contribuito al raggiungimento di questo traguardo e per questo meritano un sincero ringraziamento.

Innanzitutto, ringrazio il Prof. Mariani per avermi accolto a KTH e coinvolto nei suoi progetti di ricerca. Il suo contributo umano, con le lunghe chiacchierate del mattino, è stato prezioso tanto quanto il suo supporto professionale. Ringrazio inoltre il Prof. Avallone e l'Ing. Grava per l'aiuto che non è mai mancato, nonostante la distanza.

Ringrazio tutti coloro con cui ho condiviso momenti indimenticabili a Stoccolma: Giulia, João, Rodrigo, Marcus, Andreas ed Edoardo. Non posso non menzionare Habbri per la casualità con cui ci siamo trovati sullo stesso aereo e per quell'improbabile scommessa su quante köttbullar avrei mangiato.

Ringrazio gli amici conosciuti durante questi anni di studio, con cui ho condiviso non solo interminabili sessioni d'esame ma anche e soprattutto momenti meravigliosi: Francesco, Andrea, Luca Angelo, Edoardo, Riccardo, Tani e Jona.

Ci sono troppi motivi per ringraziare Rose, Cino, Stewe e Davi. Mi limito a dire che essere vostro amico è un grande privilegio che spero non cambi mai. Ringrazio Alessandro, con cui ho avuto la fortuna di condividere molti dei miei ricordi d'infanzia.

Il ringraziamento più importante va alla mia famiglia. A mia sorella, che nonostante le tante differenze che ci contraddistinguono sarà sempre un punto di riferimento. Ad Ariel, per sembrare l'unico labrador anaffettivo di questo mondo, ma che in realtà capisce e trasmette vicinanza al momento del bisogno. E ai miei genitori: raggiungere questo traguardo mi riempie di orgoglio, ma niente è più importante di diventare una persona di valore almeno la metà di quanto lo siate voi. Grazie per tutto il supporto e l'affetto che mi avete regalato.

Abstract

Bio-inspired designs are widely adopted in the aerodynamic design of lifting elements such as wings or propellers to enhance performance. One such design, derived from the tubercles found on the pectoral fins of humpback whales, has shown potential as a passive flow control device by manipulating flow patterns. Tubercles generate localized vortices at their leading edge, promoting an earlier transition of the laminar boundary layer to turbulent. Depending on the Reynolds number, this can delay stall and improve the overall aerodynamic performance of lifting surfaces. This is why humpback whales can perform fast, tight-turning manoeuvres despite their large mass and dimensions.

This thesis focuses on the application of tubercles, modelled in a sinusoidal shape, to the leading edge of a 30-centimeter diameter propeller, intended for use in drone and UAV propulsion systems. Small-scale propellers work within a Reynolds number range where laminar separation bubbles can form, causing performance losses due to flow separation and negatively impacting aeroacoustic behaviour. The goal of the thesis is to investigate the effects of tubercles on the overall performance of this propeller, analysing their impact on the laminar separation bubble, which has been previously studied by other researchers. The analysis is conducted using the commercial CFD code ANSYS Fluent, investigating the suitability of the Multiple Reference Frame approach, commonly used in turbomachinery and propeller simulations, to achieve this goal.

The thesis is structured into six chapters. Chapter 1 reviews the current literature on bio-inspired tubercles applications and their effects. Chapters 2 and 3 provide an overview of propeller design and characteristics, followed by a description of the turbulence and transition models used to solve the fluid dynamics equations. In Chapter 4, the CFD simulation setup of the baseline propeller is presented to verify and validate the accuracy of the numerical model. In Chapter 5, the modified propeller design, incorporating tubercles along the leading edge, is developed and simulated. Finally, conclusions and potential future work are discussed in Chapter 6.

Contents

Nomenclature

$\boldsymbol{\alpha}$	Angle of attack
$\boldsymbol{\alpha}_{stall}$	Stall angle
$\boldsymbol{\theta}$	Pitch angle
$\boldsymbol{\mu}$	Dynamic viscosity
$\boldsymbol{\rho}$	Density
$\boldsymbol{c}$	Chord
$\boldsymbol{C_D}$	Drag coefficient
$\boldsymbol{C_L}$	Lift coefficient
$\boldsymbol{C_{L_{max}}}$	Maximum lift coefficient
$\boldsymbol{C_Q}$	Torque coefficient
$\boldsymbol{C_T}$	Thrust coefficient
$\boldsymbol{D}$	Propeller diameter
$\boldsymbol{J}$	Advance Ratio
MRF	Multiple Reference frame (steady-state method)
$\boldsymbol{n}$	Angular velocity [RPS]
$\boldsymbol{r}$	Radial coordinate
$\boldsymbol{R}$	Tip radius
$\boldsymbol{Q}$	Torque
RBM	Rigid Body Motion (unsteady-state method)
Re	Numero di Reynolds
$\boldsymbol{T}$	Thrust
$\boldsymbol{V_\infty}$	Free stream velocity

List of Figures

VI

List of Tables

Chapter 1

Introduction

Bio-inspired design has gained significant attention in various engineering fields, in particular in fluid mechanics. One interesting example is the application of tubercles, small rounded bumps used along the leading edge of lifting surfaces such as wings or blades of propellers and turbines. These protuberances, shown in Figure 1.1, are inspired by the pectoral fins of Humpback Whales (*Megaptera novaeangliae*), which can perform fast, tight-turning manoeuvres despite their large mass and dimensions. For this reason, this bio-inspired concept has been studied for its potential as a passive flow control device, in order to enhance aerodynamic and hydrodynamic performance by manipulating flow behavior and delaying stall.

Figure 1.1: The Humpback Whale (*Megaptera novaeangliae*) and a zoomed-in view of the pectoral fin with tubercles [1]

1.1   State of the art

Research on leading edge tubercles began in the '90s, when scientists tried to understand Humpback Whales' surprising maneuverability. Initially, researchers attributed this ability to the bumps found on the leading edge of their elongated flippers. A great contribution to this topic was given by Fish and Battle [7], who provided a detailed description of the geometry of a Humpback Whale's pectoral fin, noticing the similarity between its cross-section and the NACA 63_4-21 airfoil. In their work, they accurately described the size and location of the tubercles, which have amplitudes ranging from 2.5% to 12% of the chord, and the distance between two adjacent peaks (or throats) in the range of 6.5% to 8.5% of the span at the mid-span of the fin. The first and biggest protuberance is located at 33% of the span, while the smallest is at 99.1% of the span. Fish and Battle were the first to hypothesize that this peculiar shape of the leading edge generates streamwise vortices that exchange momentum with the boundary layer, delaying stall and enhancing lift, particularly at high angles of attack. Thanks to their study, the potential of tubercles in aerodynamic design began to be explored.

Miklosovic et al. [8] conducted wind tunnel tests using scale models of a Humpback Whale flipper, with and without leading edge tubercles. The models, based on a NACA 0020 airfoil, were tested at a Reynolds number $Re = \bar{c}V_\infty/\nu \sim 5 \cdot 10^5$, where $\bar{c}$ is the mean chord, V_∞ is the free stream velocity and ν is the kinematic viscosity of air. Since the Reynolds number of the Humpback Whale's fin during lunge-feeding is approximately 10^6, this work can be considered reliable for young animals. Their results demonstrated a significant delay in stall for the artificial flipper with tubercles compared to that without, increasing the stall angle α_{stall} by 40% and the maximum lift coefficient $C_{L_{max}}$ by 6%. At high angles of attack, a decrease in drag was also observed, leading to an improvement in the efficiency and post-stall characteristics. The same flipper models were modelled in CFD by Weber et al [9] and Carreira Pedro and Kobayashi [10], who employed Reynolds-Averaged Navier-Stokes (RANS) equations and Detached Eddy Simulation (DES), respectively. Both studies produced results in line with experimental data in the pre-stall region. However, only DESs were able to accurately predict the flow behind the flipper after the stall, highlighting the limitations of RANS equations in predicting such a complex turbulent flow.

Experimental and numerical works showed how leading edge tubercles affect performance, but the mechanisms behind how they affect flow physics are still under investigation. Rostamzadeh et al. [11] proposed nine different hypotheses. The most accredited one is the tubercles' ability to modify the flow field by generating streamwise counter-rotating vortices between the peaks of two adjacent protuberances, energizing the boundary layer and preventing premature flow separation,

improving performance at high angles of attack. This results in a delay of flow separation or a more gradual stall behavior, depending on the Reynolds numbers and the dimensions of tubercles.

The effect of the size of tubercles on performance was studied bt Johari et al. [3], who performed water tunnel tests of rectangular wings based on the NACA 63$_4$-21 profile, with and without leading edge tubercles, to understand the underlying fluid dynamics. They analyzed three tubercle amplitudes of 0.025c, 0.05c, and 0.12c with two wavelengths of 0.25c and 0.50c at $Re = 1.83 \cdot 10^5$. Figure 1.2 shows how amplitudes and wavelengths are defined. Their experiments revealed that the performance of the wings with leading edge tubercles, in terms of lift and drag, was worse compared to the smooth wing. However, after the stall, the lift of the modified wings was up to 50% higher than the baseline wing, with no increase in drag (Figure 1.3). Flow visualization showed that the stall primarily occurred in the throats at all angles of attack, while the flow remained attached behind the peaks up to high angles of attack, where the baseline wing already exhibited flow separation. They also found that performance and flow separation depend especially on the amplitude of the protuberances rather than the wavelength. Similar results were obtained by Hansen et al. [12], who studied the effect of tubercles with various amplitudes and wavelengths on wings based on NACA 0021 and NACA 65-021 airfoils. Larger tubercle amplitudes generated a smoother stall behavior, though they reduced the maximum lift coefficient $C_{L_{max}}$ and the stall angle. In contrast, smaller amplitudes achieved a higher $C_{L_{max}}$ and an increased stall angle among all the modified wings and exhibited better post-stall performance compared to the unmodified model.
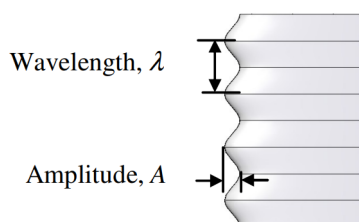
Figure 1.2: Definition of amplitude and wavelength [2]

1.1.1 Application of tubercles in propellers

The effect of leading edge tubercles was explored not only on wings but also on marine and aeronautical propellers to study how they affect performance. Ibrahim and New [1] numerically investigated with ANSYS Fluent the use of tubercles on a marine propeller. Using a Multiple Reference Frame approach with a realizable $k - \epsilon$ Turbulence Model, they demonstrated that the thrust coefficient could be
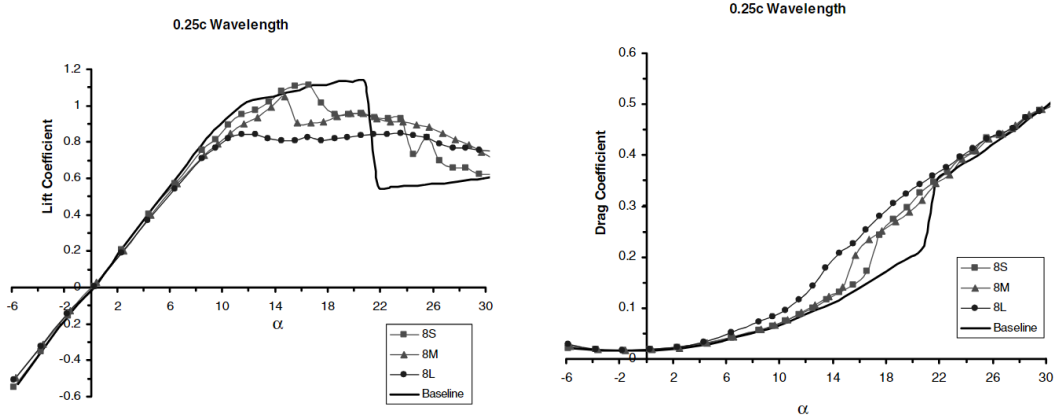
Figure 1.3: Lift and Drag coefficients of NACA 63_4-21 airfoil with and without tubercles leading edge [3]. S, M and L indicate the amplitude of the tubercles

improved by up to 10%, at the cost of an approximately 10% increase in the torque coefficient, resulting in an overall decrease in efficiency.

The study conducted by Stark et al. [13] investigated how tubercles affect cavitation, a critical issue that is typical of marine propellers. Their work showed this bio-inspired modification applied on a ducted Kaplan propeller can mitigate cavitation, significantly improving propeller performance and durability.

Aeronautical propellers were studied by Butt and Talha [14], who conducted a numerical analysis of the effects of leading edge tubercles on performance. They tested various amplitudes and wavelengths by scaling the chord length of the reference propeller. The amplitude was set to 0.1c and 0.2c, with wavelengths of 3% and 8.5% of the span, resulting in four different configurations. Simulations were performed with rotational velocities in the range of 4 000 to 10 000 RPM and 5 different advance ratios were considered. All modified configurations showed higher efficiency across all advance ratios, except at $J = 0.8$, where reverse thrust was observed. Tubercles with larger amplitudes and shorter wavelengths showed the greatest increase in efficiency, as it was hypothesized that they generate stronger counter-rotating chordwise vortices between adjacent peaks.

1.1.2 Application at low Reynolds number

Leading edge tubercles have also been investigated at low Reynolds numbers. Stanway [15] conducted tests on a model of a whale flipper across a Reynolds number range of 44 000 to 120 000. His study revealed that the model with tubercles was characterized by a lower lift coefficient in the pre-stall region compared to the smooth version.

Leading edge tubercles were applied to a wing based on NACA 0021 airfoil at $Re = 120\,000$ by Hansen et al. [2], who tested various amplitudes and wavelengths. They observed that performance improved significantly in the post-stall regime, while a lower lift coefficient was measured before the stall with respect to the unmodified wing. An interesting thing they found was that the lift coefficient of the baseline wing presented an increased slope after 4°, attributed to the formation of a Laminar Separation Bubble, which virtually increased the wing camber. Moreover, this baseline wing was characterized by a sudden and strong stall. In contrast, the modified wing showed a lower $C_{L_{max}}$, but a much smoother post-stall behavior. In terms of drag, the modified wing performed similarly to the smooth model before the stall, except near the stall angle, where the leading edge tubercles caused a higher drag coefficient. However, after the stall, drag was lower compared to the smooth version. Among the configurations tested, the smallest amplitude, equal to 3% of the chord length, with the biggest wavelength, equal to 11% of the chord length, provided the highest maximum lift coefficient and stall angle and improved lift after stall. Generally, performance improved by decreasing the wavelength of the tubercles, up to a point where further reductions no longer enhanced the performance.

1.2   Purpose of this thesis

The goal of this thesis is to investigate the application of bio-inspired leading edge tubercles on a small-scale propeller with a diameter of 30 centimeters, suitable for using in drone and UAV propulsion systems. This type of propellers operates within a chord-based Reynolds number range of 10^4 to 10^5, where a Laminar Separation Bubble (LSB) can form on the suction side of the blades, compromising performance and negatively impacting aeroacoustic behavior.

In this work, the leading edge tubercles were designed as a sinusoidal shape and two different design methodologies were explored. The effect of this modification on the flow field around the blades was studied through CFD simulations, which were carried out with the commercial software ANSYS Fluent. Special attention was given to the influence of the tubercles on the formation, position and length of LSBs. The thesis also evaluated the capability of the Multiple Reference Frame (MRF) approach, commonly used in turbomachinery and propeller simulations, to simulate propellers within this Reynolds number range, with and without protuberances.

By examining the aerodynamic effects of tubercles and comparing the Baseline Propeller with its modified counterpart, the research aims to understand whether

this bio-inspired modification can be used as a passive flow control device on small-scale propellers. The outcomes could offer practical insights for improving the performance of propellers in drones and UAVs.

Chapter 2

Propellers design and aerodynamics

Propellers convert the mechanical torque power of the shaft into forward or reverse axial thrust, depending on the operation point, thanks to their capability to accelerate the working fluid, which may be air or water, used respectively for aircraft or marine vehicles. Propellers were the first type of propulsion for aircraft, dating back to the first flight by the Wright brothers on December 17, 1903. Since then, research on propeller design and aerodynamics never stopped, and nowadays this device is gaining increasing popularity due to the growing use of helicopters, UAVs, and drones of various scales and configurations. This chapter aims to provide an overview of propeller design and aerodynamics.

2.1 Geometric characteristics

To understand how a propeller works and the aerodynamics of this device, it is essential to define some geometric characteristics and their terminology, such as pitch and the angles involved in the flow field around the blades. Moreover, an overview of the parameters used to define propeller performance is presented.

Pitch

The pitch of a propeller is the distance it would advance along the axis of spinning in one revolution if the propeller is thought of as a screw moving along a helix with an angle equal to its blade angle [16]. The geometrical pitch may differ from the experimental pitch, which is the distance the propeller would actually advance in one revolution providing zero thrust.

Propellers can be divided into two main categories:

- **Fixed-pitch propellers**, characterized by a pitch that does not vary during aircraft operation. The maximum efficiency is reached at only one advance ratio, but they are the cheapest propellers to install on an aircraft.

- **Variable-pitch propellers**, characterized by blades that can rotate around their axis to vary the pitch. This type of propeller allows maintaining the optimum angle of attack and therefore the optimum efficiency. However, they are more expensive in terms of manufacturing and maintenance costs.

Pitch angle θ

The pitch angle θ is the angle between the chord of a section of the blade and the plane of rotation of the propeller. Since the tangential velocity of the blade changes along the blade span, θ varies along the radius to maintain the optimum angle of attack.

Angle of attack α

The angle of attack α is the angle between the chord of a section of the blade and the relative velocity impinging on it. This angle is defined as:

$$\alpha = \theta - \phi \tag{2.1}$$

where ϕ is the angle between the relative velocity impinging on the blade section and the plane of rotation of the propeller. Assuming the rotation and the aircraft velocities are constant, the tangential velocity varies proportionally to the radius of the blade as $V_t = \omega R$ and, as a consequence, ϕ varies along the radius. To a first approximation, the relative velocity is defined as:

$$V_{rel} = \sqrt{V_t^2 + V_\infty^2} \tag{2.2}$$

where V_∞ is the aircraft or free stream velocity. This approximation does not take into account the tangential and axial induction coefficients, but it can be useful to have a rough estimation of the relative velocity. This means that α is also a function of the freestream velocity (or advance ratio J). Figure 2.1 shows the velocity triangles for a fixed-blade section at two different freestream velocities. It is evident that increasing the aircraft velocity (increasing the advance ratio J), the ϕ angle decreases and consequently α decreases as well. Therefore, the maximum thrust is obtained when $V_\infty = 0$, i.e. $J = 0$, and there is a specific advance ratio where the thrust is zero: a further increase in the freestream velocity would lead to negative thrust.

8
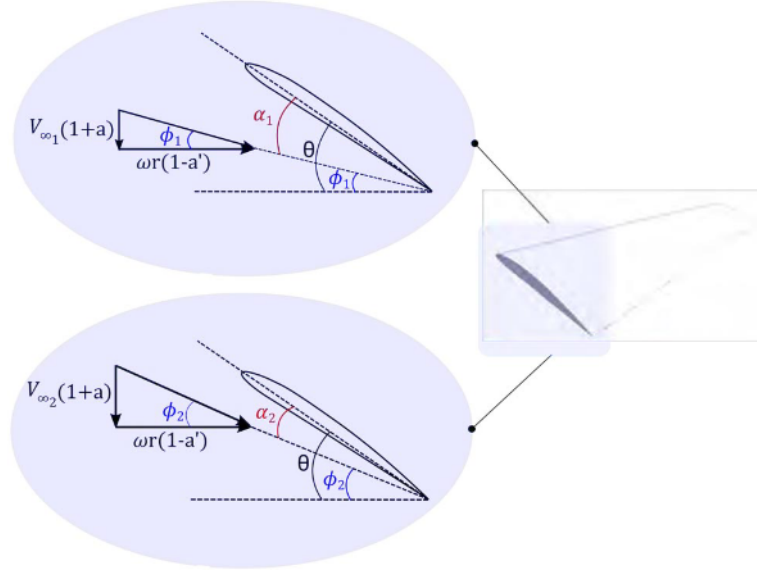
Figure 2.1: Velocity triangles for a fixed-pitch propeller blade section at two different freestream velocities [4]

2.2 Performance

Fixed-pitch propeller performance depends on the following parameters:

- The diameter of the propeller (D).

- Working fluid properties, such as the density ρ, the dynamic viscosity μ, and the static temperature T, that defines the speed of sound a.

- The angular velocity n, expressed in revolutions per second (RPS). The same rotation rate can be named Ω and expressed in rad/s.

- The freestream velocity V_∞, usually equal to the aircraft velocity.

The quantities used to define propeller performance are the thrust T and the torque Q. Ideally, the best propeller generates the maximum Thrust with the minimum Torque, that corresponds to the mechanical power to provide to the shaft. As is usually done in fluid dynamics, thrust and torque can be expressed through dimensionless parameters to better compare different scenarios characterized by similar flow phenomena. In the following, a list of useful dimensionless quantities is presented.

- Reynolds number: assuming the freestream and the rotational velocities are constant, this parameter is a function of the radius of the blade.

$$Re(r) = \frac{\rho V_{rel}(r)c(r)}{\mu} \tag{2.3}$$

9

where $c(r)$ is the local chord length of the blade cross-sections along the radius. As a first approximation, V_{rel} can be computed as in (2.2). However, for a greater accuracy, the tangential and axial induction coefficients should be taken into account. It is common practice to define a representative Reynolds number at a radial position of $r/R = 0.6$ or $r/R = 0.75$, where R is the blade tip radius.

- Mach number: this parameter is important to predict whether the flow field around the blade is subsonic or supersonic, especially at the tip where the velocity is maximum

$$M = \frac{V_{rel}}{a} = \frac{V_{rel}}{\sqrt{\gamma R^* T}} \tag{2.4}$$

- Advance ratio: at the same value of this parameter, every blade section of the propeller will experience the same angle of attack, even while changing the freestream and/or the rotational velocities.

$$J = \frac{V_\infty}{nD} \tag{2.5}$$

- Thrust coefficient:

$$C_T = \frac{T}{\rho n^2 D^4} \tag{2.6}$$

- Torque coefficient:

$$C_Q = \frac{Q}{\rho n^2 D^5} \tag{2.7}$$

- Efficiency:

$$\eta = \frac{C_T J}{2\pi C_Q} \tag{2.8}$$

Propeller performance is usually defined by the the curves $C_T(J, Re, M)$ and $C_Q(J, Re, M)$; as a consequence, a curve for $\eta(J, Re, M)$ is present. The dependance on the the advance ratio is always present in a fixed-pitch propeller performance. The dependance on the Reynolds number must be taken into account when the scale of the propeller is small or the rotational velocity is low. In such scenario, the Reynolds number along the blade span is low, therefore the viscous effects are not negligible with respect to the inertial effects. The dependance on the Mach number must be taken into account when the rotational velocity is high enough to lead to a compressible flow field around the blade ($M > 0.3$). If the spinning velocity is sufficient high, the tip of the blade may be encounter a transonic flow and generate a shock wave.

2.3   Momentum theory

The momentum theory, also called disk actuator theory, is the simplest method to estimate the propeller performance, though it neglects the flow field near the blades and focuses only on the integral quantities such as thrust and torque. This theory, based on the work of Rankine and Froude, describes the propeller like a circular disk, characterized by an infinite number of blades, where the thrust is uniformly distributed. Therefore, the propeller is considered as having an infinitesimal thickness, which is mathematically modelled as a surface discontinuity. The momentum theory is based on the following hypotheses:

- Stationary and irrotational flow.

- Inviscid flow.

- Incompressible flow.

- Velocity and static pressure are assumed to be uniform over each side of the disk. Pressure at infinity upstream and infinity downstream is equal to the ambient pressure.

- The rotation of the flow field due to the torque is neglected. Therefore, possible discontinuities in the tangential component of the velocity are not allowed.

These assumptions allow resolving the flow field using Euler's equations. As shown in figure 2.2, consider an air flow of velocity V_∞ impinging normally on a surface of diameter D. The mass flow must be continuous, but pressure discontinuities are allowed. According to the conservation of energy, the change in flow momentum between upstream and downstream of the disk is equal to the thrust produced by the propeller.
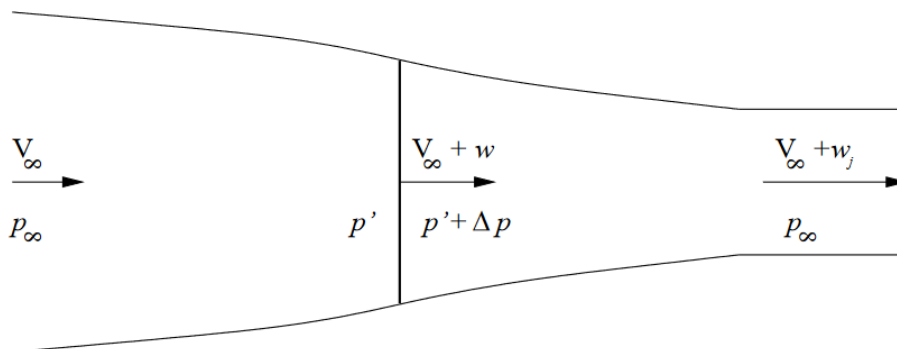

Figure 2.2: Disk actuator theory [5]

11

The flow is irrotational except accross the disk, where a pressure discontinuity is present, therefore it is possible to apply Bernoulli's equation to the flow field upstream and downstream of the disk.

$$\begin{cases} p_1^o = p_\infty + \frac{1}{2}\rho V_\infty^2 = p' + \frac{1}{2}\rho \left(V_\infty + w\right)^2 \\ p_2^o = p_\infty + \frac{1}{2}\rho \left(V_\infty + w_j\right)^2 = p' + \Delta p + \frac{1}{2}\rho \left(V_\infty + w\right)^2 \end{cases} \qquad (2.9)$$

Subtracting the two equations:

$$p_2^o - p_1^o = \Delta p = \rho w_j \left(V_\infty + \frac{1}{2}w_j\right) \qquad (2.10)$$

As mentioned earlier, the force applied by the flow to the surface is equal to the change in flow momentum between upstream and downstream of the disk. At the same time, thrust is equal to the pressure increase behind the surface multiplied by the area A of the disk.

$$T = \Delta p A = \dot{m} w_j = \rho A \left(V_\infty + w\right) w_j \qquad (2.11)$$

Substituting the value of Δp in the above equation, it is possible to compute the *induced velocity at the disk*:

$$w = \frac{1}{2}w_j \qquad (2.12)$$

i.e., the *induced downstream velocity* is double the induced velocity at the disk. Now, substituting (2.12) in (2.11), it is possible to rewrite the thrust as:

$$T = 2\rho A \left(V_\infty + w\right) w \qquad (2.13)$$

The power P is the work done on the fluid by the propeller, modelled as a surface discontinuity, and it can be expressed as the difference in the kinetic energy accross the disk:

$$P\Omega Q = \dot{m} \left[\frac{1}{2} \left(V_\infty + w_j\right)^2 - \frac{1}{2}V_\infty^2\right] = T \left(V_\infty + w\right) \qquad (2.14)$$

The ideal efficiency of the propeller can be defined as:

$$\eta = \frac{TV_\infty}{P} = \frac{1}{1 + \frac{w}{V_\infty}} = \frac{1}{1 + a} \qquad (2.15)$$

where $a = w/V_\infty$ is the *axial induction coefficient*. From this equation, it is evident that in order to increase the efficiency, a must be reduced, which can be achieved by increasing the propeller diameter. However, the ideal efficiency obtained does not take into account the viscous effects of the flow, the rotational kinetic energy, and the fact that the thrust is not actually uniform over the disk surface. For this reason, the momentum theory is capable of computing the ideal or limiting propeller performance.

Effects of wake rotation

The fifth hypotesis presented in the previous section concerns the rotation of the flow field within the wake, which is neglected. This means that only axial velocity variations are considered, while variations in radial and tangential velocities are not taken into account. However, the rotation of the propeller with angular velocity Ω induces a rotational velocity downstream of the disk. Betz developed an extension of the momentum theory to account for this phenomenon. In his work, the viscous effects are still neglected, therefore the ideal efficiency computed with the general momentum theory, i.e. Betz's theory, must be considered the maximum value that a real propeller cannot exceed. A more detailed explanation of this theory can be found in [5] and [17].

Chapter 3

Numerical modeling

In the thesis, the propeller under investigation and its leading edge tubercle modification have been studied using Computational Fluid Dynamics (CFD). Specifically, the Reynolds-Averaged-Navier-Stokes (RANS) equations and their unsteady counterpart uRANS have been solved. Both are derived from the Navier-Stokes equations by applying a statistical approach to account for turbulence. In these equations, the instantaneous flowfield is decomposed into a time-averaged (mean) component and a fluctuating component (turbulence fluctuations):

$$u = \bar{u} + u' \tag{3.1}$$

By substituting this decomposition into the Navier-Stokes equations and averaging over time, an additional term emerges: the Reynolds stress tensor $\overline{u_i' u_j'}$. This term represents the influence of the turbulence fluctuations on the mean flow and it introduces additional unknowns. Because of that, the number of unknowns is greater than the number of equations. To find a solution, turbulence models are required to correlate these terms to the mean flow quantities. Thanks to Boussinesq's *eddy viscosity* hypothesis and Prandtl's concept of the *mixing length*, several turbulence models have been developed. The most popular models are the one-equation *Spalart-Allmaras* [19] and the two-equation models $k - \omega$ and $k - \epsilon$. For this thesis, the SST $k - \omega$ has been employed, as its suitability for computing small-scale propeller performance has been demonstrated in [20, 21]. Due to the nature of the propeller flow field under investigation, characterized by the presence of a laminar separation bubble on the suction side of the blades (see Chapter 4 for further details), different transition models were also tested and are discussed later in this Chapter.

3.1   Steady and Unsteady state approaches

The flow field around a propeller is intrinsically unsteady due to the rotation of the blades. Therefore, the most intuitive method to simulate such a problem is to set up

a time-dependent simulation, where the rotating domain (containing the propeller) spins, along with the mesh. However, ANSYS Fluent and other CFD commercial software offer two distinct techniques for simulating the flow around a propeller: the steady-state *Multiple Reference Frame* (MRF) approach and the unsteady-state *Rigid Body Motion* (RBM) approach, that handles the actual rotation of the domain and its mesh [26]. The choice of approach depends on the simulation goals and the available computational resources.

Multiple Reference Frame

The Multiple Reference Frame approach transforms an intrinsically unsteady problem in the stationary reference frame into a steady problem in a moving reference frame. If capturing transient phenomena is not necessary, such as when estimating propeller performance at its optimal design point, the Navier-Stokes equation can be solved in a rotating reference frame centered at the axis of rotation, spinning at the same velocity as the propeller. The computational domain must be divided into two regions: a stationary region, where the fluid motion equations are solved in the global stationary reference frame, and a rotating region containing the propeller, where the equations are solved in the rotating reference frame. In both zones, the flow is assumed to be steady-state, meaning that unsteady effects caused by the rotation are not considered. This method is computationally efficient because it avoids the mesh rotation and does not require solving the uRANS equations, which are computationally more expensive than RANS equations. However, the MRF approach is limited to problems where the computational domain is axisymmetric and the free stream velocity is aligned with the axis of the rotation of the rotating region.

Rigid Body Motion

The Rigid Body Motion approach, also known as Sliding Mesh, is an unsteady method that takes into account the actual motion of the moving component. This allows to capture transient effects, making it the most accurate approach for simulating rotating components. Like in the Multiple Reference Frame approach, to simulate a propeller the computational domain must be divided into stationary and rotating regions. The difference is that with this method the rotating region (and its mesh) physically rotates with respect to the stationary part, using uRANS equations and updating the mesh at each time step. However, the computation cost is significantly higher compared to the MRF approach. If the primary goal is the time-averaged behavior of the rotating component and computational resources are limited, the Multiple Reference Frame approach can be used. On the other hand, if transient phenomena must be computed, the Rigid Body Motion approach should be taken into consideration, keeping in mind the increased computational cost.

3.2   SST $k - \omega$ turbulence model

The Shear Stress Transport $k - \omega$ turbulence model is a two-equation model developed by Menter [22] to improve accuracy in simulations involving adverse pressure gradients and flow separation. Like Wilcox's original $k - \omega$ model [18], it solves two separate transport equations: one for the turbulent kinetic energy k and one for the specific dissipation rate ω.

The original model suffers of strong sensitivity to free stream conditions, therefore the SST $k - \omega$ model blends the $k - \omega$ predictions near the wall with the independence from the free stream conditions of the $k - \epsilon$ model in the far field. This is achieved through a blending function that equals to one near walls, activating the $k - \omega$ model, and goes to zero in the free stream region, where the $k - \epsilon$ model is preferred. Another feature of the SST $k - \omega$ model is the Shear Stress Transport (SST) modification, which limits the turbulent viscosity to prevent the model from over-predicting turbulence growth at stagnation points. This modification improves performance in regions with strong adverse pressure gradients or flow separation.

This turbulence model has the advantage of being versatile and able to predict the onset and extent of flow separation. For this reason, and considering its relatively low computational cost, it is a good choice for many industrial applications.

3.3   Transition models

Turbulence models like those mentioned in the previous section are designed for fully turbulent flows. However, when the laminar-to-turbulent transition needs to be accurately predicted, transition models become essential. This section provides an overview of the transition models used later in the thesis to compute the flow field around the propeller.

$\gamma - Re_\theta$ Transition Model

The $\gamma - Re_\theta$ model, referred to as the *SST transition* model in ANSYS Fluent, is a four-equation transition model developed by Langtry and Menter [24, 25]. It is based on the SST $k - \omega$ model, coupled with two additional transport equations: one for Intermittency γ and one for a transition onset criterion based on the momentum-thickness Reynolds number Re_θ. The Intermittency describes the percentage of the flow that is turbulent at any given location, increasing from zero to one as the flow goes from laminar to turbulent. The second term is related to the Reynolds number at which transition begins.

The propeller under investigation is characterised by the presence of a Laminar Separation Bubble on the suction side of the blades. For this reason, a transition model like the $\gamma - Re_\theta$ must be considered to predict the laminar separation and the turbulent reattachment. However, this model is based on empirical transition correlations that are not Galilean invariant, meaning it can only be applied with a steady-state MRF approach.

γ-Algebraic Transition Model

The γ-Algebraic model is a more computationally efficient alternative to the $\gamma - Re_\theta$ model and it is part of the family of Local-Correlation-based transition models. Instead of solving a transport equation for γ, Intermittency is computed through an algebraic equation. Moreover, the transport equation for Re_θ is omitted, as it has been observed that the convection-diffusion terms are negligible compared to the source terms [26].

Due to its low computational cost, the γ-Algebraic model is a good choice when a first estimation of transition is needed, such as during preliminary designs. Unlike the $\gamma - Re_\theta$ model, this model can be applied with an unsteady state approach, allowing both the transitional and unsteady characteristics of the flow field to be computed.

Chapter 4

Verification and validation

This chapter focuses on the verification and validation of the numerical model used to simulate the small-scale propeller operating at low Reynolds numbers chosen as the reference. A 3D scan of a commercially available propeller would have provided limited geometric data, leading to less accurate flow simulations. Additionally, the aerodynamic and performance data of such propellers are often sparse, not allowing an accurate validation. Therefore, for this thesis, a reference propeller that has been extensively studied and documented was selected, due to the availabilty of detailed geometric, aerodynamic and aeroacoustic data, both experimental and numerical. By validating the numerical methods used in this work against the well-documented data of this specific propeller, confidence in the accuracy of the simulations for subsequent analysis of the effects of leading edge tubercles has been established.

4.1   Baseline Propeller

The propeller selected as the reference, referred to as the Baseline Propeller (Figure 4.1) in the following, is well documented in several studies [4, 27–29]. This propeller was designed at TU Delft specifically to study low Reynolds numbers flow regimes, making it suitable for drones or UAV propulsion systems. It is a modified version of a commercially available propeller. The base geometry was derived from an APC 9×6 model, a two-bladed aircraft propeller with a 9-inch (22.86 cm) diameter and a 6-inch (15.24 cm) pitch. The diameter was then scaled up to 30 cm, and the airfoil along the blade was modified to a NACA 4412 profile. Near the root, an elliptical section was incorporated, which smoothly transitions into the airfoil section starting from a radial distance of 1 cm from the hub center. The distribution of chord length and pitch angle of the blade over the radial distance is illustrated in Figure 4.2, along with the Reynolds number distribution, computed without accounting for the tangential and axial induction coefficients.
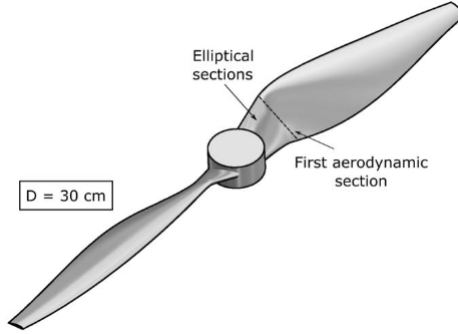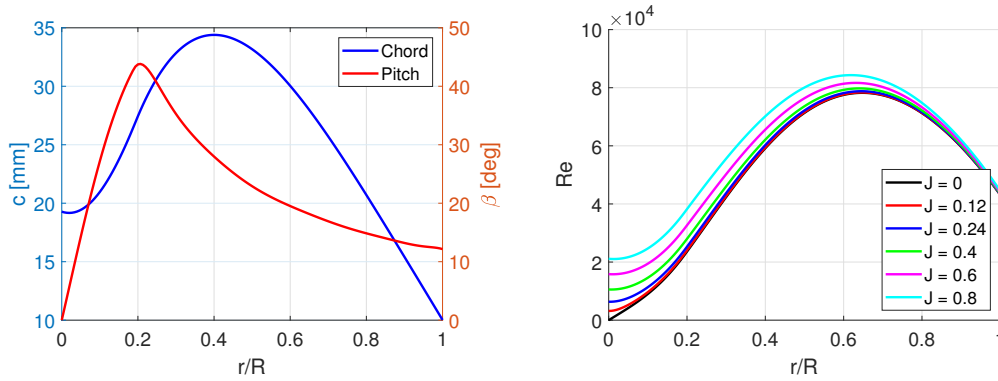
Figure 4.1: Baseline Propeller geometry [4]

Figure 4.2: Baseline Propeller blade's chord length, pitch angle and Reynolds number distribution

The studies mentioned above provide an extensive analysis of the flow field around the blades, both experimentally, thanks to oil-flow visualizations and phase-locked stereoscopic PIV measurements, and numerically. Because of the propeller's low Reynolds number operating regime, laminar separation occurs on the suction side of the propeller blades and the separated shear layer is subjected to a turbulence transition, leading to reattachment and the formation of a Laminar Separation Bubble (LSB). The location of the LSB depends on the angle of attack, shifting toward the leading edge as the angle of attack increases, which corresponds to lower advance ratios. At higher advance ratios, when the angle of attack decreases, the laminar separation moves downstream and the turbulence reattachment, if present, occurs close to the trailing edge of the blade. LSBs have several consequences for airfoil performance [6], and similarly affects propeller performance. From an aerodynamic perspective, they can increase drag and reduce lift, particularly at higher angles of attack where the adverse pressure gradient is larger. Behind Laminar Separation Bubbles, vortex shedding can form, increasing flow unsteadiness and acoustic emissions. To better visualise how an LSB can form, Figure 4.3 shows the streamlines around a conventional airfoil at different Reynolds numbers.
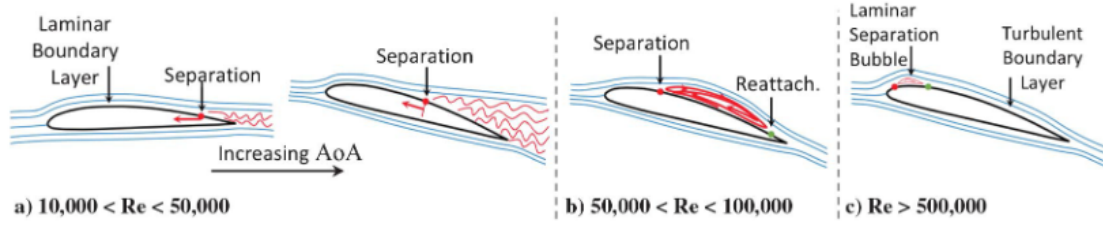
Figure 4.3: Flow field around a conventional airfoil at different Reynolds numbers [6]

All the experimental results used in the following sections to validate the numerical model are based on tests conducted in the A-tunnel at TU Delft. For those experiments, the propeller was manufactured with aluminum alloys using computer numerical control (CNC) machining, in order to ensure high precision and a surface roughness of 0.4 to 0.8 μm Ra, which enhanced the quality of the aerodynamic flow around the blades, leading to more reliable experimental data. Additionally, the use of aluminium alloys provided high stiffness, resulting in minimal vibrations and elastic deformations during the tests.

4.2   Fluid domain and solver selection

The CFD simulations were set up using ANSYS Fluent. The computational domain was divided into two regions: a stationary region and a rotating region. The stationary region consists of a cylinder coaxial with the propeller, large enough to allow the proper development of the wake and to minimize the impact of boundary conditions on the flow. The domain has a diameter of $8D$, where $D = 300$ mm is the diameter of the Baseline Propeller, and a length of $15D$. The inflow surface is positioned $5D$ upstream from the propeller center, while the outflow surface is $10D$ downstream. The propeller is located at the center of the rotating region, which is a cylinder with a diameter of $1.15D$ and a length of $0.4D$. These dimensions were defined according to the rotating region sensitivity analysis reported in [20].

For all advance ratios, a *Velocity Inlet* boundary condition was applied at the inflow of the domain, with the inlet turbulence intensity set to 0.1%, accordin to the experimental data obtained in the anechoic A-tunnel at TU Delft [4]. At the outflow, a *Pressure Outlet* boundary condition with zero gauge pressure was imposed to allow the wake to develop without reflection. The backflow turbulence intensity was set to 0.1%. The propeller surfaces were modelled as *No-Slip Walls*.

For advance ratios $J > 0$, the lateral boundaries of the domain were modelled as *Slip Walls*, in line with what has been found in [20], which showed that with

20

such a large domain, the boundary condition applied at the lateral boundaries does not affect thrust and torque coefficient.

For the hovering case ($J = 0$), a *Velocity Inlet* boundary condition was applied at the lateral boundaries, with a free stream velocity of 0.05 m/s. This small inflow velocity was necessary to reach convergence, as a free stream velocity equal to zero would have caused tip vortices to spread laterally, compromising the accuracy of the solution [21]. This adjustment corresponds to an advance ratio of $J = 0.0025$.

Since the Reynolds number at a fixed radial position on the blade primarily depends on the rotational velocity, this parameter was kept constant at 4000 RPM for all simulations. To vary the advance ratio, the free stream velocity was adjusted, so that the Reynolds number at the chosen radial position remained approximately constant. At this rotational speed, even at the highest advance ratio, the tip Mach number was lower than 0.3, so the flow can be treated as incompressible. The range of advance ratios analyzed is shown in Table 4.1.

Table 4.1: Advance ratios and free stream velocities

$\mathbf{J}$	$\boldsymbol{V_\infty}$ [m/s]	$\mathbf{n}$ [RPM]
0.0025	0.05	4000
0.12	2.4	4000
0.24	4.8	4000
0.4	8	4000
0.6	12	4000
0.8	16	4000

The Moving Reference Frame (MRF) approach was employed to simulate the propeller rotation. A comparison with the Rigid Body Motion (RBM) approach is presented in Section 4.5.1 to further validate the model. The simulations were performed using the pressure-based solver, suitable for incompressible flows. The SIMPLE algorithm was used for pressure-velocity coupling, and second-order accuracy was applied to both the momentum and pressure equations to enhance the fidelity of the solution. Standard sea-level conditions were assumed for the operating environment:

$$p = 101325\,Pa \quad \rho = 1.225\,kg/m^3 \quad \mu = 1.789 \times 10^{-5}\,Pa \cdot s$$

4.3 Mesh independence analysis

For the simulations, initial tetrahedral meshes were generated and then converted into polyhedral grids to improve numerical accuracy and reduce computational

cost, allowing easier convergence. To ensure that the results were not influenced by mesh density, a mesh independence study was performed. Four different meshes were tested, varying in element count and refinement near the propeller blades and in critical flow regions. Special attention was paid to the boundary layer around the blades to capture the near-wall flow behavior accurately. Additionally, a fine mesh density in the wake region behind the propeller was applied to properly capture vortex shedding and flow separation. For this reason, a cylindrical refinement was applied, using a clylinder coaxial with the propeller with a diameter of $1.5D$, extending $0.5D$ upstream and $2D$ downstream. The key parameters for each mesh are summarized in Table 4.2. *Mesh 1* and *Mesh 2* mainly differ in boundary layer cell refinement: *Mesh 1* has a y^+ in the range of 10 to 30, while *Mesh 2* has a $y^+ \sim 0.1$. *Mesh 2*, *Mesh 3* and *Mesh 4* have the same boundary layer y^+, with a progressive increase in mesh density.

Table 4.2: Mesh parameters

	Mesh 1	Mesh 2	Mesh 3	Mesh 4
Total elements	2 136 298	10 244 867	11 236 911	14 362 476
	Stationary region			
Minimum cell size	10 mm	10 mm	3 mm	2 mm
Maximum cell size	100 mm	100 mm	100 mm	100 mm
Growth rate	1.2	1.2	1.2	1.2
	Rotating region			
Minimum cell size	2.5 mm	2.5 mm	1.5 mm	1 mm
Maximum cell size	10 mm	10 mm	3 mm	2 mm
Growth rate	1.2	1.2	1.2	1.15
	Blades refinement			
Minimum cell size	0.1 mm	0.1 mm	0.1 mm	0.1 mm
Maximum cell size	1 mm	1 mm	0.75 mm	0.5 mm
Trailing Edge	4.5e-2 mm	4.5e-2 mm	4.5e-2 mm	4.5e-2 mm
Growth rate	1.2	1.2	1.2	1.2
	Boundary Layer			
$\boldsymbol{y^+}$	$\sim$ 10-30	$\sim$ 0.1	$\sim$ 0.1	$\sim$ 0.1
First layer height	0.2608 mm	2.8e-3 mm	2.8e-3 mm	2.8e-3 mm
Layers	6	26	26	26
Growth rate	1.1	1.2	1.2	1.2
	Wake refinement			
Maximum cell size	25 mm	25 mm	15 mm	10 mm

The advance ratios $J = 0.0025$ and $J = 0.6$ were selected for the mesh independence analysis, as they represent the conditions with the highest angle of attack and

the highest efficiency, respectively. The analysis was performed with a steady-state approach (MRF), using the SST $k-\omega$ turbulence model and comparing the Thrust and Torque coefficients across the four meshes.

Table 4.3 shows the relative error in Thrust and Torque coefficients with respect to *Mesh 4*, the finest mesh. The results from *Mesh 1*, with a y^+ greater than 1, show a distance of about 7% for the Thrust coefficient at both advance ratios and nearly 3% for the Torque coefficient at $J = 0.6$. However, *Mesh 2* and *Mesh 3*, with a y^+ below 1, provided more accurate results, with errors consistently below 2% for *Mesh 2* and below 0.3% for *Mesh 3*. Having $y^+ < 1$ is crucial for accurately predicting the boundary layer, especially at low Reynolds numbers. The mesh independence analysis demonstrated that beyond 11 236 911 elements, further refinement did not significantly affect the results. Therefore, *Mesh 3* was selected for the simulations as it offered the best balance between accuracy and computational cost. Figure 4.4 shows the mesh of the computational domain, along with a zoomed-in view of the mesh at the blade section located at a radial coordinate of $r/R = 0.6$.

Table 4.3: Relative error in Thrust and Torque coefficients with respect of the finest mesh

$J = 0.0025$		
Mesh	C_T	C_Q
1	-7.01%	6.07%
2	-1.51%	1.54%
3	-0.19%	0.21%

$J = 0.6$		
Mesh	C_T	C_Q
1	-6.84%	2.92%
2	-0.55%	-0.16%
3	-0.16%	-0.07%

An interesting detail that deserves to be mentioned is that unexpected oscillations in Thrust and Torque were observed at $J = 0.0025$ when y^+ was below 1, meaning that full convergence was not achieved. This may be related to the unsteady nature of the flow behind the Laminar Separation Bubble. The unsteadiness is likely more pronounced at this advance ratio, since the angle of attack is maximum. Further validation using a Rigid Body Motion approach was carried out and is discussed later in this Chapter to better understand whether the results provided by the MRF approach at this advance ratio are reliable.
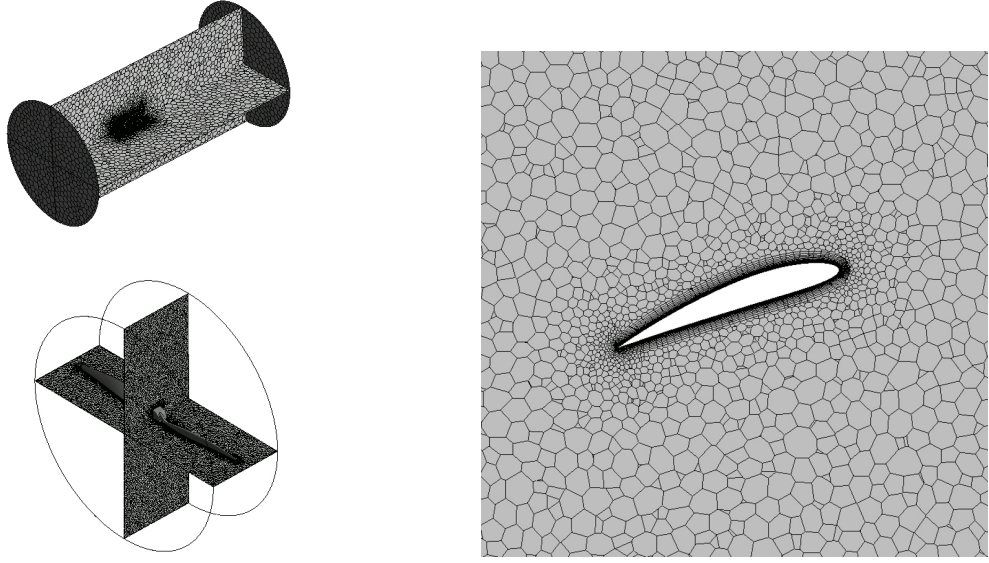
Figure 4.4: Baseline Propeller computational domain and mesh

4.4 Transition models comparison

To accurately capture the laminar separation and the turbulent reattachment, a detailed comparison of two different transition models was conducted with a steady-state approach (MRF). The goal was to identify which model best replicates the complex flow phenomena occurring at the low Reynolds numbers typical of the Baseline Propeller. Initially, the SST $k - \omega$ turbulence model was used without any transition model. Subsequently, it was coupled with the $\gamma - Re_\theta$ Transition Model and the γ-Algebraic Transition Model. The performance of these models was evaluated against experimental data by comparing Thrust and Torque coefficients, as well as by evaluating their ability to predict the Laminar Separation Bubble over the propeller blades. As in the mesh independence analysis, the advance ratios $J = 0.0025$ and $J = 0.6$ were selected for this comparison. The relative errors in Thrust and Torque coefficients (Table 4.4) show that the $\gamma - Re_\theta$ Transition Model significantly underpredicts the performance of the Baseline Propeller at $J = 0.6$, underestimating C_T by almost 23% and C_Q by nearly 12%. For this reason, this transition model was not considered suitable for further simulations. The SST $k - \omega$, without a transition model, provided the most accurate results at both advance ratios, slightly overestimating Thrust and Torque at $J = 0.0025$ and underestimating them at $J = 0.6$. The γ-Algebraic Transition Model showed a similar trend but with slightly larger errors.
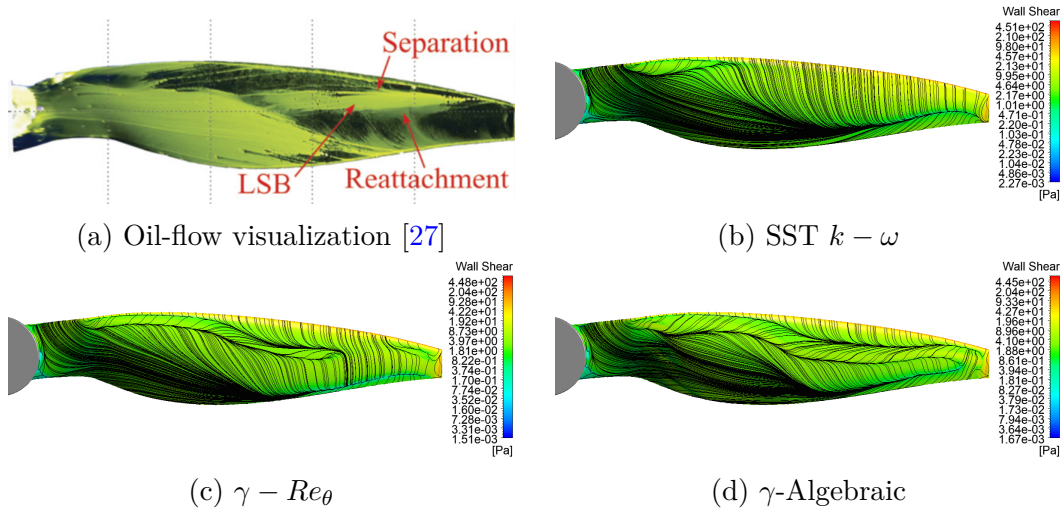
Surface streamlines on the blade's suction side were compared with the oil-flow visualization from [27] to evaluate whether the turbulence and transition models

24

Table 4.4: Relative error in Thrust and Torque coefficients with respect to experimental data for different transition models

$J = 0.0025$		
Turbulence model	**C_T**	**C_Q**
SST $k - \omega$	5.36%	0.61%
SST $k - \omega + \gamma - Re_\theta$	9.37%	2.36%
SST $k - \omega + \gamma$-Algebraic	6.87%	1.80%

$J = 0.6$		
Turbulence model	**C_T**	**C_Q**
SST $k - \omega$	-7.52%	-1.53%
SST $k - \omega + \gamma - Re_\theta$	-22.90%	-11.60%
SST $k - \omega + \gamma$-Algebraic	-9.18%	-4.35%

captured the LSB. The results are shown in Figures 4.5 and 4.6 for $J = 0.0025$ and $J = 0.6$, respectively. Additionally, the pressure coefficient over the blade cross-section at a radial position of $r/R = 0.6$ was compared with the PIV data reconstruction from [4] and is presented in Figure 4.7.

(a) Oil-flow visualization [27]

(b) SST $k - \omega$

(c) $\gamma - Re_\theta$

(d) γ-Algebraic

Figure 4.5: Comparison of surface streamlines on the blade suction side at $J = 0.0025$ with different transition models and experimental oil-flow visualization

Although the SST $k - \omega$ and the γ-Algebraic produced similar results in terms of C_T and C_Q, the surface streamlines revealed that the SST $k - \omega$ is not able to capture the Laminar Separation Bubble that occurs on the propeller blades. In contrast, the γ-Algebraic Transition Model accurately predicted both the laminar

(a) Oil-flow visualization [27]

(b) SST $k - \omega$
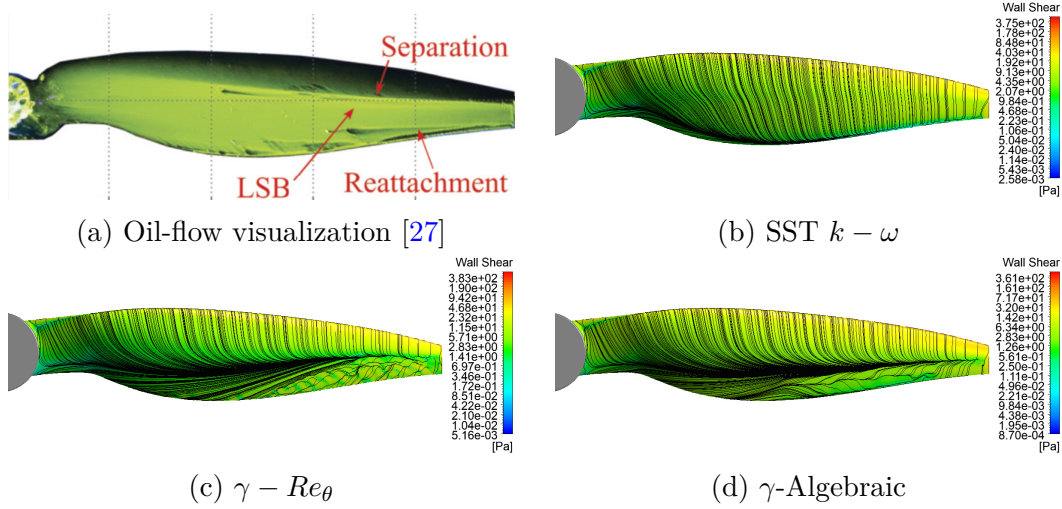
(c) $\gamma - Re_\theta$

(d) γ-Algebraic

Figure 4.6: Comparison of surface streamlines on the blade suction side at $J = 0.6$ with different transition models and experimental oil-flow visualization
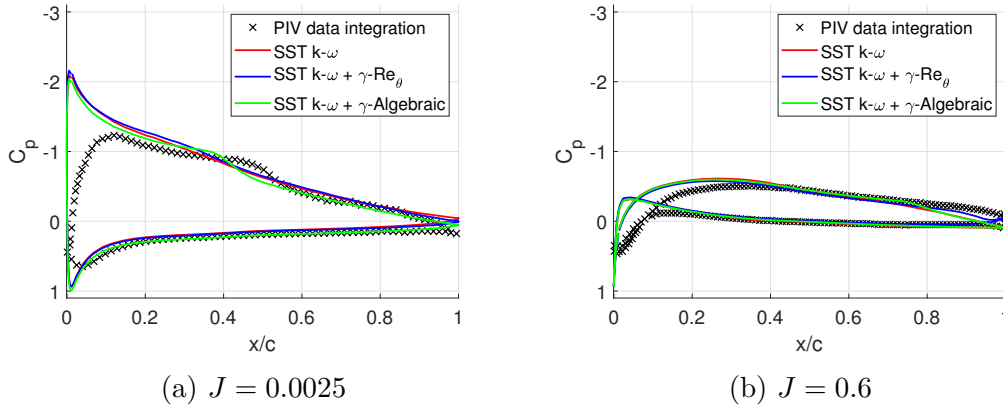

(a) $J = 0.0025$

(b) $J = 0.6$

Figure 4.7: Comparison of the pressure coefficient over the blade cross-section at $r/R = 0.6$ with different transition models and PIV data reconstruction

separation at both advance ratios and the subsequent turbulent reattachment at $J = 0.0025$. The pressure coefficient plots were in line with the surface streamlines results, as the LSB manifests as a pressure plateau followed by a pressure rise, which is not evident in the SST $k - \omega$ results but is captured by the PIV data reconstruction. The γ-Algebraic Transition Model successfully predicted these phenomena, although it did not exactly match the reattachment location. The comparison of the pressure coefficient with the PIV data reconstruction showed good agreement, particularly on the pressure side for both advance ratios. On the suction side, the pressure coefficient was slightly overestimated and differences were more pronounced at the leading edge, but considering that PIV data reconstructions cannot

26

be considered as perfectly accurate due to inherent limitations in spatial resolution and data processing, the results provided by the γ-Algebraic Transition Model were considered reliable. Consequently, this transition model was chosen for subsequent simulations.

4.5   Results

Simulations were extended to cover a wider range of advance ratios. Table 4.5 and Figure 4.8 show C_T, C_Q, and η, while Table 4.6 reports the relative errors with respect to experimental data.

Table 4.5: Mean values and standard deviations of C_T, C_Q, and η for the Baseline Propeller, computed using the steady-state approach

J	0.0025	0.12	0.24	0.4	0.6	0.8
C_T	0.1185	0.1094	0.0972	0.0734	0.0353	-0.0085
$\sigma_{C_T} \cdot 10^3$	0.5995	0.0657	0.0465	0.0264	0.0187	0.0168
C_Q	0.0077	0.0080	0.0081	0.0073	0.0048	~ 0
$\sigma_{C_Q} \cdot 10^3$	0.5073	0.0710	0.0310	0.0110	0.0256	0.0230
η	/	6.40%	3.35%	2.34%	-5.05%	-132.76%

Table 4.6: Relative error in performance coefficients with respect to experimental data for the Baseline Propeller

J	0.0025	0.12	0.24	0.4	0.6	0.8
C_T	6.87%	5.37%	3.63%	-0.35%	-9.18%	-87.12%
C_Q	1.80%	-0.97%	0.27%	-2.63%	-4.35%	-19.61%
η	/	6.40%	3.35%	2.34%	-5.05%	-132.76%

Results indicate that the CFD simulations overestimated the Thrust Coefficient at lower advance ratios, particularly from $J = 0.0025$ to $J = 0.24$, and underestimated it at higher advance ratios. The Torque Coefficient showed good agreement with experimental data, with a relative error consistently below 4.5% up to $J = 0.6$. However, the numerical simulations struggled to predict propeller performance accurately at $J = 0.8$, where reverse thrust occurs. Considering the uncertainty in the experimental thrust and torque measurements from [4], the relative error in C_T compared to the upper limit of the error bars drops to 4.8% for $J = 0.0025$ and 3.6% for $J = 0.12$. The standard deviations of C_T and C_Q in hovering are an order of magnitude greater than those at all other advance ratios, due to unexpected oscillations, indicating that full convergence was not achieved. Further validation

27

(a) Thrust Coefficient

(b) Torque Coefficient

(c) Efficiency
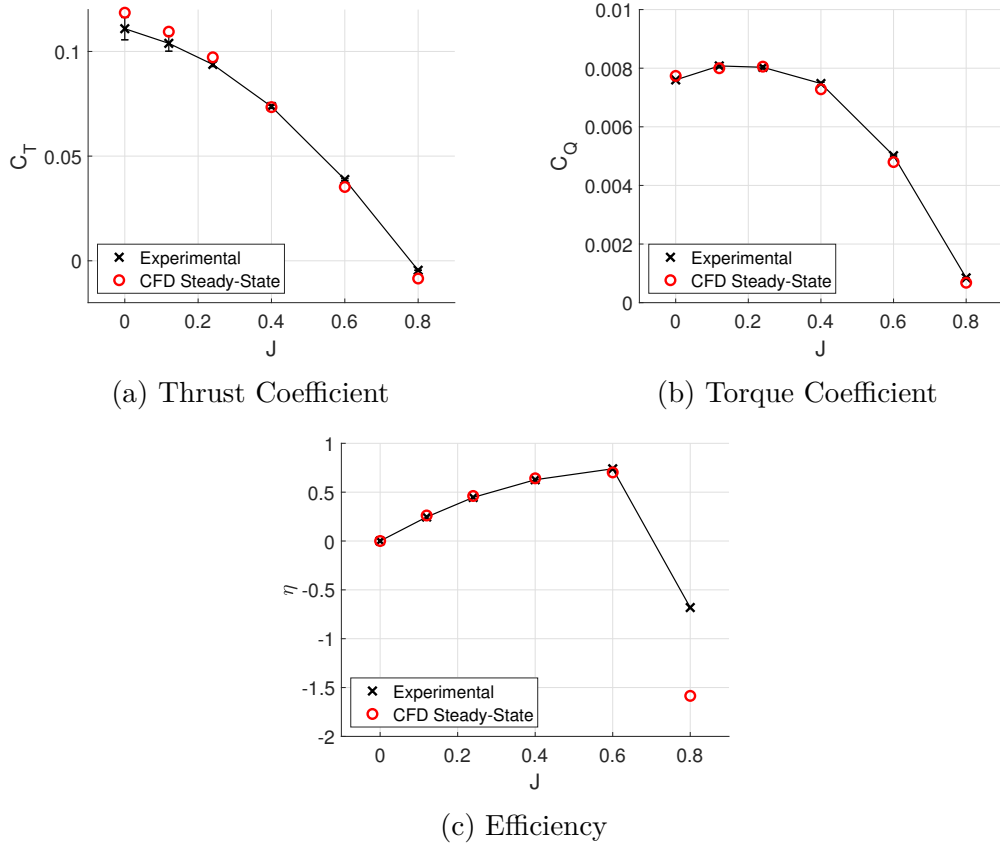
Figure 4.8: Plots of C_T, C_Q, and η for the Baseline Propeller

with the unsteady-state approach is discussed in Section 4.5.1. In conclusion, the Multiple Reference Frame approach with the γ-Algebraic Transition Model is suitable for computing the performance coefficients of the Baseline Propeller in terms of C_T and C_Q.

Surface streamlines were compared with oil-flow visualization from [4] and Lattice-Boltzmann/Very-Large Eddy-Simulation Simulation results from [27] in Figures 4.9 and 4.10. The results show good agreement, mostly at higher advance ratios, between the surface streamlines predicted by the CFD simulations and both the experimental and numerical references. The simulations performed with the MRF approach successfully captured the Laminar Separation Bubble for advance ratios from $J = 0.0025$ to $J = 0.4$. For $J = 0.6$, the simulations detected the laminar separation, but it is unclear if a turbulent reattachment was computed. As reported in the literature, the laminar separation point moves toward the leading edge as the advance ratio decreases.

(a) $J = 0.0025$

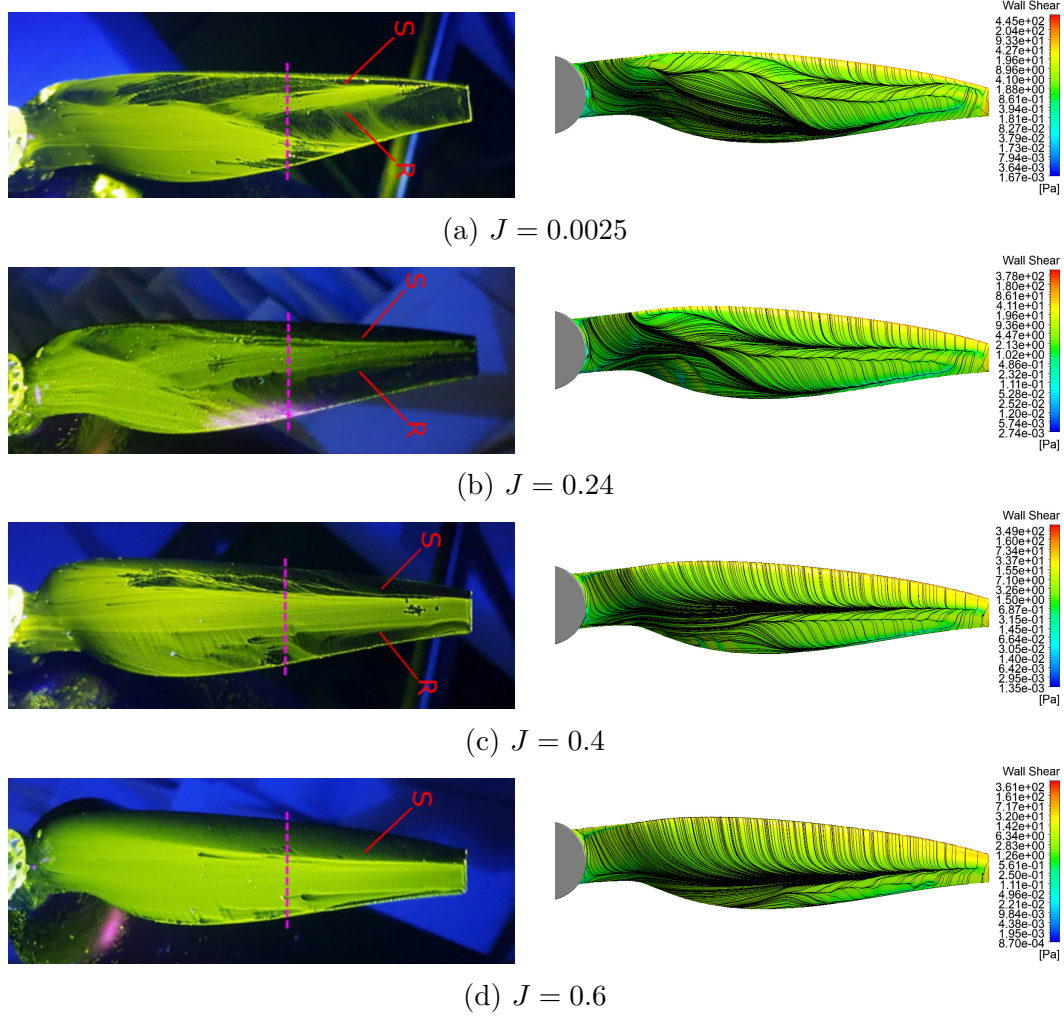(b) $J = 0.24$

(c) $J = 0.4$

(d) $J = 0.6$

Figure 4.9: Comparison of surface streamlines on the blade suction side and experimental oil-flow visualization [4]

The length and location of the LSB were further investigated by analyzing the pressure and skin friction coefficients (Figures 4.11 and 4.12, respectively) over three different blade cross-sections located at $r/R = 0.4$, $r/R = 0.6$ and $r/R = 0.8$. On a conventional airfoil, the skin friction coefficient in the chordwise direction typically becomes negative when the flow separates and returns to positive if reattachment occurs. However, due to the presence of strong radial flow over the propeller blades, this simple correlation between the sign of the skin friction coefficient and the state of the flow (attached or separated) is not directly applicable, but it still helps to qualitatively estimate the nature of the flow and possibly the location of flow separation and reattachment.
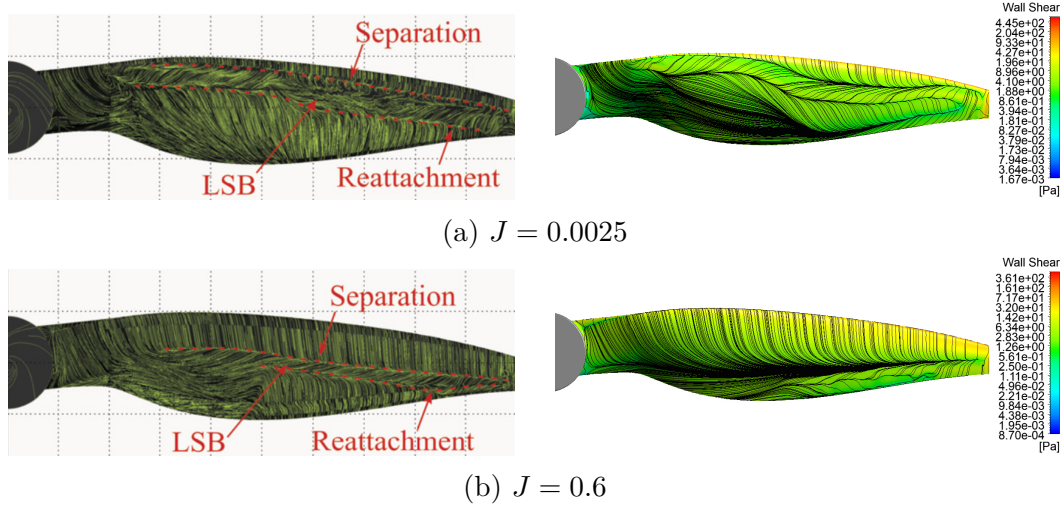
(a) $J = 0.0025$

(b) $J = 0.6$

Figure 4.10: Comparison of surface streamlines on the blade suction side and LBM numerical simulations [27]

The results are in line with the surface streamlines predictions, confirming that the MRF approach combined with the γ-Algebraic Transition Model captured the flow behavior around the Baseline Propeller. The comparison of the pressure coefficient with PIV data reconstruction shows good agreement, particularly on the pressure side for all advance ratios. On the suction side, the pressure coefficient is slightly overestimated in all cases, with differences more pronounced at the leading edge, especially for lower advance ratios, where the pressure peak is higher due to larger angles of attack. The LSB manifests as a pressure plateau, observable across all advance ratios. The subsequent pressure rise is linked to turbulent reattachment, though the simulations consistently underestimate the reattachment location compared to the experimental data, but considering the uncertainties in PIV data acquisition and processing, the simulation results are considered reliable. Both the pressure coefficient and the skin friction coefficient indicate that the Laminar Separation Bubbles shift downstream as the advance ratio increases. Despite the significant radial flow present over the propeller blades, the skin friction coefficient remains a valuable indicator of whether the flow is attached or separated, as the negative values of c_f align with the locations of the pressure plateaus.
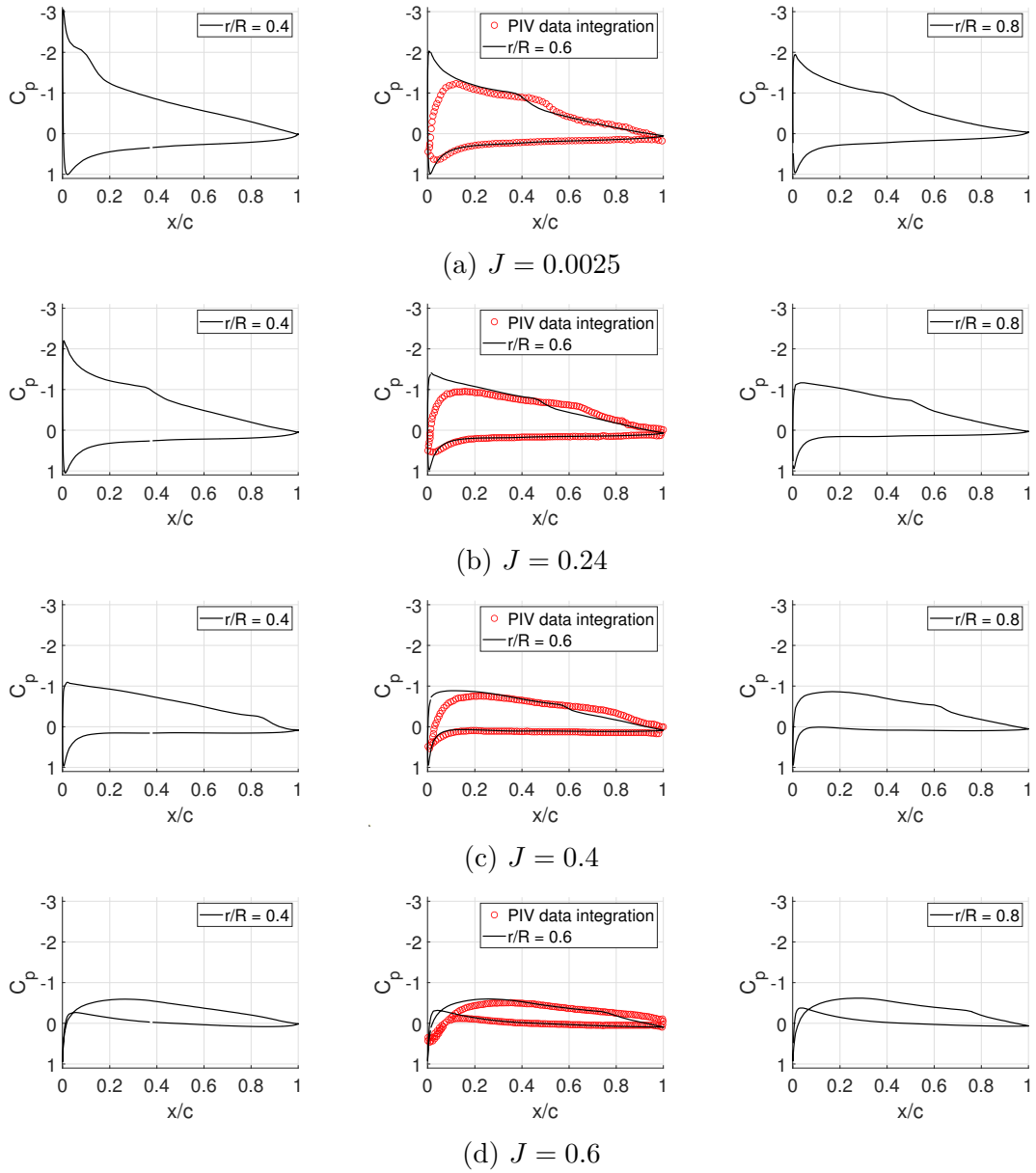
(a) $J = 0.0025$

(b) $J = 0.24$

(c) $J = 0.4$

(d) $J = 0.6$

Figure 4.11: Pressure coefficient over 3 different Baseline Propeller's blade cross-sections

31

(a) $J = 0.0025$

(b) $J = 0.24$

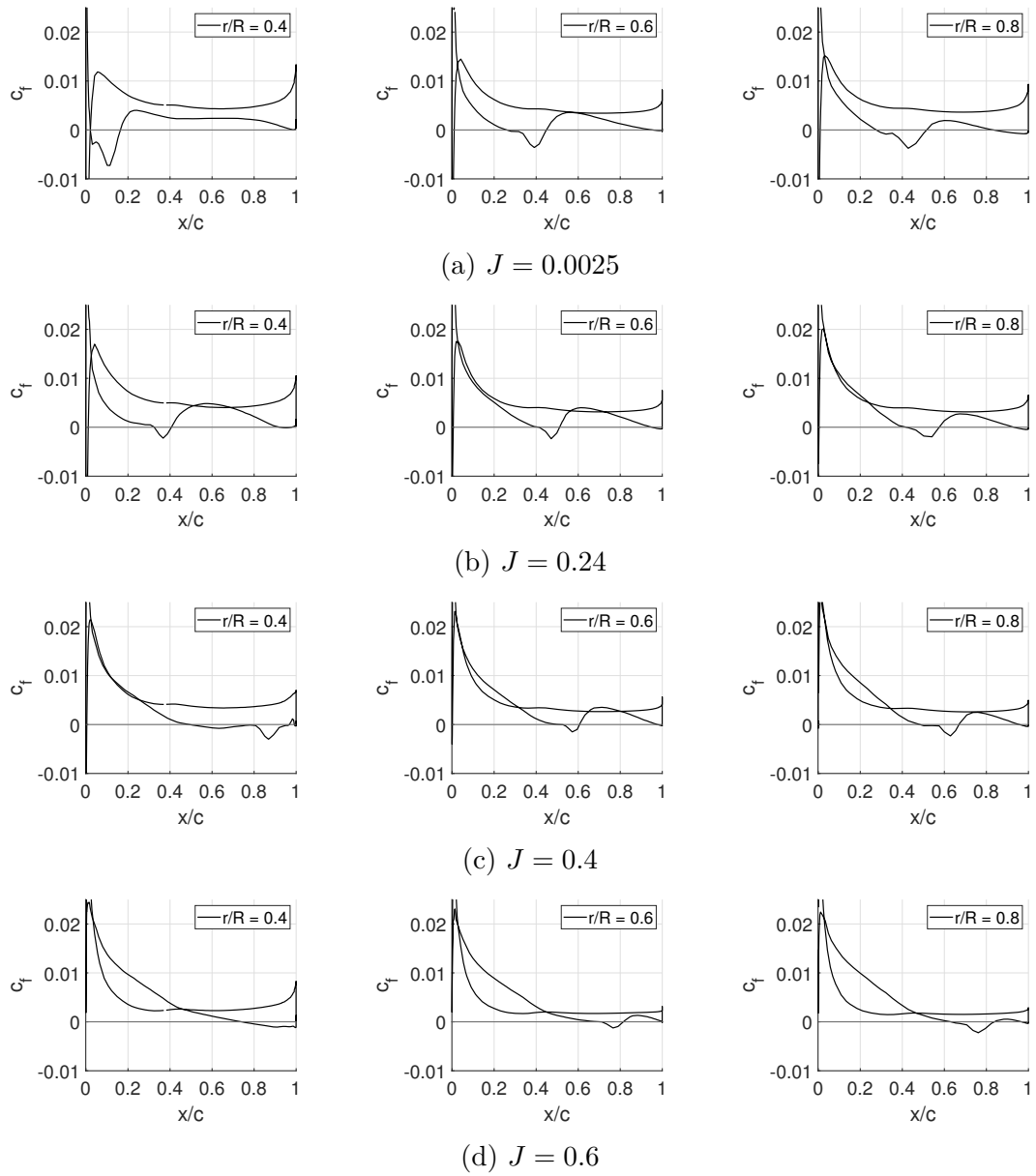(c) $J = 0.4$

(d) $J = 0.6$

Figure 4.12: Skin friction coefficient over 3 different Baseline Propeller's blade cross-sections

4.5.1 Unsteady-State simulations

The unsteady-state approach (RBM) was also used in order to obtain an additional layer of validation for the numerical model. Infact, this method offers a more realistic representation of the blade motion and captures the unsteady behavior of the flow field, while the Multiple Reference Frame is limited to time-averaged values. To run the simulations, an implicit solver was selected, configured with a second-order bounded scheme in order to maximize stability and accuracy in capturing the flow dynamics over time. The time step was set to correspond to the time required by the propeller to rotate by one degree.

The results shown in Table 4.7 indicate that both methods produced similar trends in thrust and torque coefficients across the range of advance ratios, demonstrating that the MRF method is a viable option for simulating propeller performance.

Table 4.7: Baseline Propeller performance computed with steady-state (MRF) and unsteady-state (RBM) methods

J	C_T			C_Q		
	MRF	RBM	Exp	MRF	RBM	Exp
0.0025	0.1185	0.1196	0.1109	0.0077	0.0079	0.0076
0.12	0.1094	0.1111	0.1039	0.0080	0.0081	0.0081
0.24	0.0972	0.0975	0.0938	0.0081	0.0081	0.0080
0.4	0.0734	0.0737	0.0736	0.0073	0.0073	0.0075
0.6	0.0353	0.0359	0.0388	0.0048	0.0049	0.0050
0.8	-0.0085	-0.0084	-0.0045	~ 0	~ 0	~ 0

J	η		
	MRF	RBM	Exp
0.0025	/	/	/
0.12	0.2613	0.2619	0.2456
0.24	0.4612	0.4625	0.4461
0.4	0.6418	0.6431	0.6271
0.6	0.7021	0.7054	0.7394
0.8	-1.5850	-1.5692	-0.6810

Instantaneous pressure and skin friction coefficients over three Baseline Propeller blade cross-sections computed with both methods are illustrated in Figure 4.13 and in Figure 4.14.
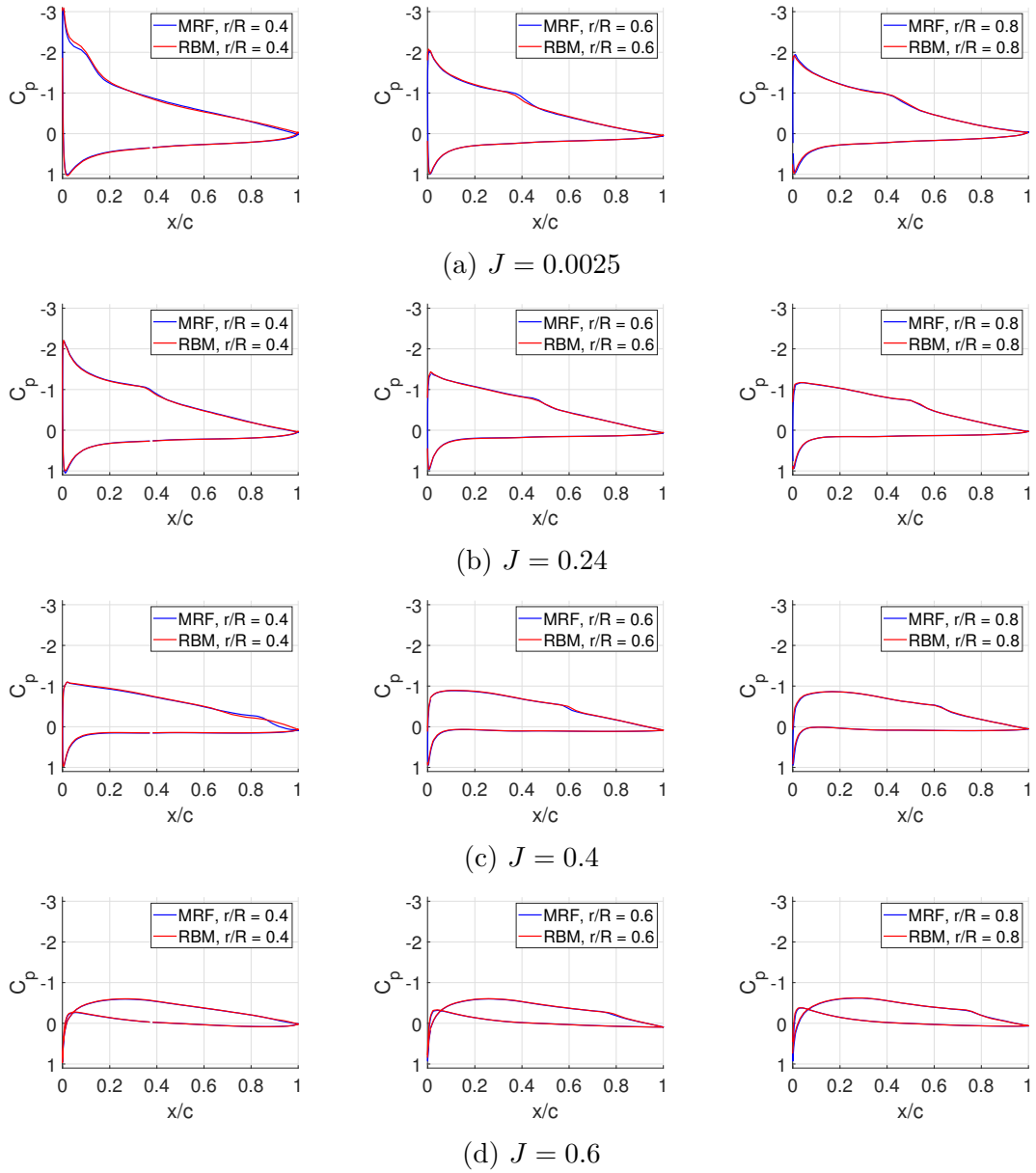
Figure 4.13: Comparison of the steady (MRF) and unsteady (RBM) approaches in term of pressure coefficient

(a) $J = 0.0025$

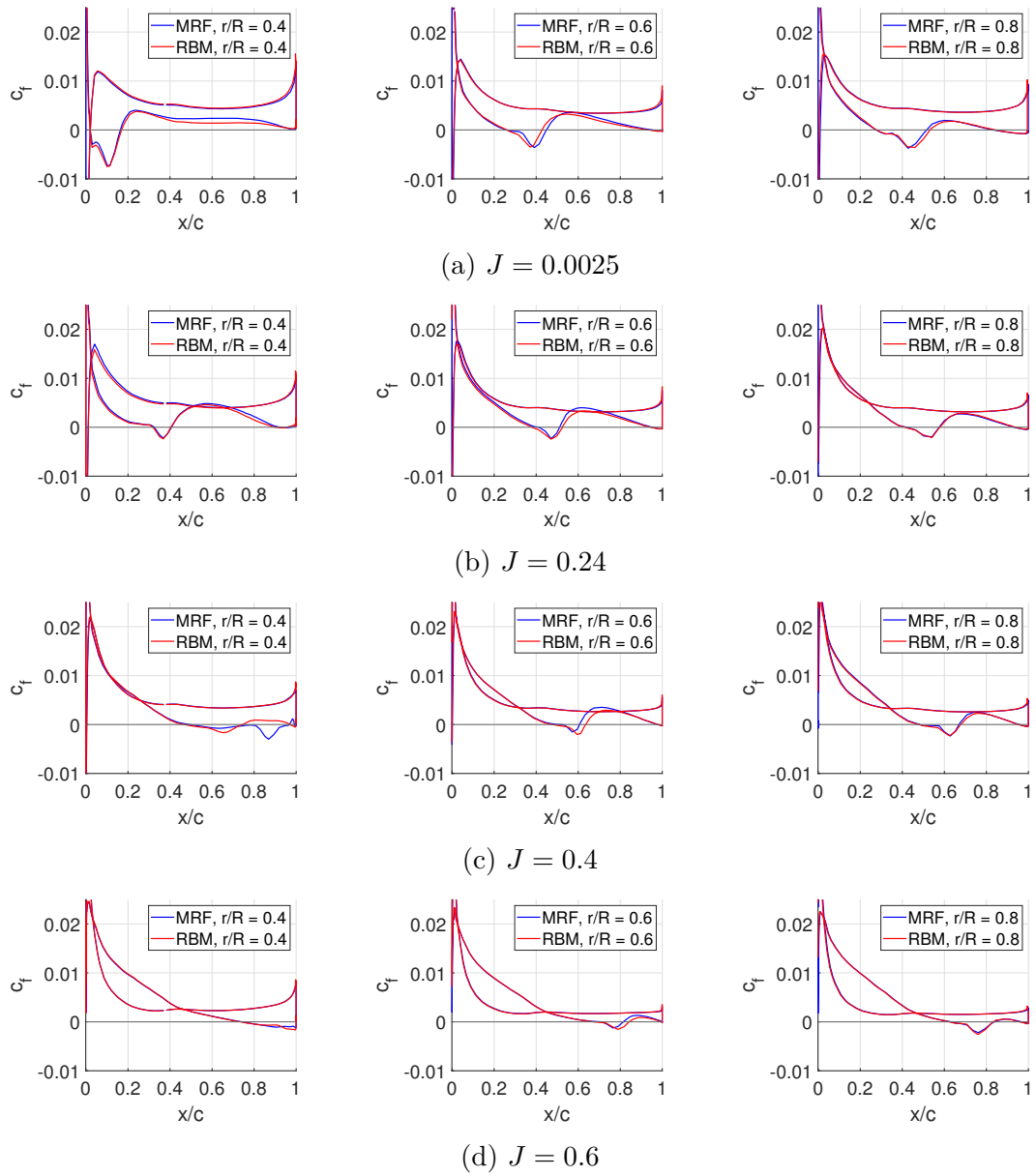(b) $J = 0.24$

(c) $J = 0.4$

(d) $J = 0.6$

Figure 4.14: Comparison of the steady (MRF) and unsteady (RBM) approaches in term of skin friction coefficient

The two approaches predicted the same behaviour of the flow around the blades, computing nearly identical pressure and shear stress distributions over the blades. The only observed difference was in the skin friction coefficient at $r/R = 0.4$ for the advance ratio $J = 0.4$. The steady-state method (MRF) computed negative shear stress in the chordwise direction on the second half of the blade section, while the unsteady-state approach (RBM) predicted a return to positive shear stress, suggesting the possibility of turbulent reattachment. However, the pressure coefficients provided by both methods for the same radial position and same advance ratio showed good agreement. Additionally, C_T and C_Q at $J = 0.4$ were accurately predicted by both methods compared to the experimental data.

The unexpected oscillations in Thrust and Torque produced by the Multiple Reference Frame method at $J = 0.0025$, discussed in Section 4.3, were attributed to the MRF's incapability to achieve full convergence. However, the Thrust and Torque coefficients computed with the Rigid Body Motion differ by less than 1% and 1.5%, respectively, from those predicted by the MRF approach. This indicates that MRF is suitable for predicting propeller performance across the entire range of advance ratios.

In conclusion, the verification and validation of the numerical model discussed in this Chapter demonstrated that the SST $k - \omega$ Turbulence Model, coupled with the γ-Algebraic Transition Model, is suitable for predicting Baseline Propeller performance using the steady-state approach on a mesh of around 11 million elements with $y^+ < 1$. The Thrust and Torque coefficients were predicted with relative errors below 5.5% and 4.5% in the range of $J = 0.12$ to $J = 0.4$. For the hovering case, the error was slightly larger, but this aligns with the uncertainties in the experimental measurements. However, for $J = 0.6$, the relative error increased and at $J = 0.8$, where reverse thrust occurs, the simulations failed to predict propeller performance. The numerical model also predicted the flow behavior around the propeller, computing a pressure distribution over the blades in line with the experimental data. The surface streamlines over the blades showed the presence of a Laminar Separation Bubble, suggesting that the γ-Algebraic Transition Model effectively predicts laminar separation and subsequent turbulent reattachment. Nonetheless, the location of turbulent reattachment was consistently underestimated for all advance ratios. Special attention must be given to the hovering case, where non-physical oscillations of C_T and C_Q can occur, suggesting that an unsteady simulation may be necessary to accurately validate propeller performance.

Chapter 5

Leading edge tubercles modification

This chapter focuses on the application of sinusoidal leading edge tubercles to the Baseline Propeller blades. Inspired by the flow control mechanisms observed in Humpback Whale flippers, this bio-inspired design aims to modify the flow behavior around the propeller and potentially enhance its performance.

5.1   Tubercles design

The design of the tubercles was based on a sinusoidal profile, with the amplitude and wavelength carefully selected to optimize flow characteristics. Since both the chord length and the pitch angle vary along the radial distance from the hub, the modification was applied by maintaining a constant ratio between the modified chord and the Baseline Propeller's chord, as described by the following equation:

$$\frac{c_{wavy}}{c_{BL}} = -A \sin\left(\frac{2\pi}{\lambda}\left(r - r_0\right)\right) + 1 \tag{5.1}$$

The parameters are defined as follows:

- **Amplitude:** $A = 0.05$. The chord length was scaled by 5%. Since the chord of the Baseline Propeller varies along the radial span, the absolute value of the tubercle amplitude changes in the same manner. This means that tubercles near the hub, where the local chord length is larger, are bigger, while those near the tip are smaller due to the reduced chord length. This value was selected to have a good balance between smaller tubercles that minimize the impact on the maximum lift coefficient and larger tubercles that produce smoother stall behavior. [2, 3, 12].

- **Wavelength:** $\lambda = 12.75\,mm$. A review of the literature [3, 12] indicated that the distance between tubercles does not significantly affect performance.

Therefore, the wavelength was set to 8.5% of the blade span, roughly corresponding to the distance between the tubercles of Humpback Whales' fins [7].

- **Starting point** $r_0 = 45\,mm$. The modification begins at 30% of the blade span, in agreement with the location of the first tubercle on a Humpback Whale's fin [7]. The transition between the unmodified section of the blade and the tubercles-modified leading edge was smoothed in Solidworks using a spline.

Figure 5.1 illustrates the ratio of the modified chord over the original chord, along with its absolute value.
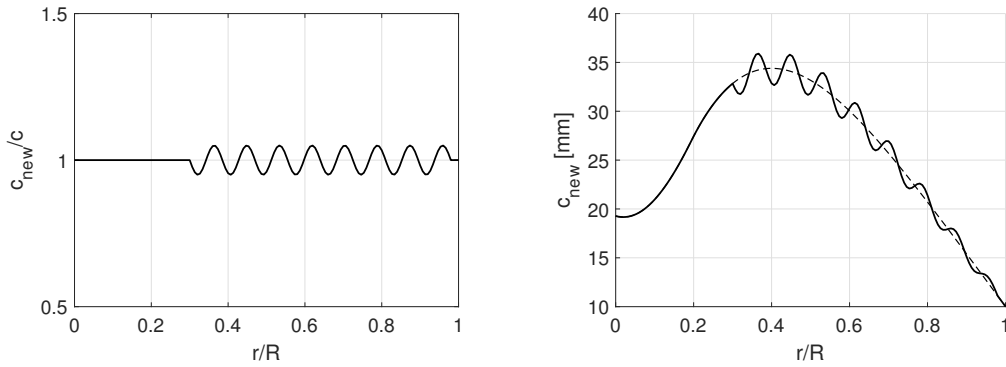

Figure 5.1: Chord length of the tubercles-modified propeller

Tubercles were applied to the propeller blades with two different methodologies. In the first design, referred to as Wavy 1, only the chordwise coordinates of the Baseline Propeller's airfoils were scaled, stretching the airfoil along its length without proportionally scaling its thickness. This resulted in a loss of the original NACA 4412 profile and a reduced local thickness-to-chord ratio. In contrast, the second design, referred to as Wavy 2, scaled both the chordwise and thickness coordinates proportionally, preserving the NACA 4412 profile. Although the differences may seem minimal, Wavy 1 changes the airfoil shape, while Wavy 2 maintains it. Figure 5.2 illustrates the modified airfoils and a zoomed-in view of the leading edge.

In both Wavy 1 and Wavy 2, the addition of leading edge tubercles creates undulations along the suction side of the airfoil, with humps behind tubercle peaks and depressions behind throats. However, this effect is more pronounced in Wavy 2 because the thickness of the original airfoil was scaled proportionally with the chord length. As a result, the sinusoidal modification introduced by the tubercles on the leading edge was also mirrored on the upper surface, amplifying the humps and depressions.
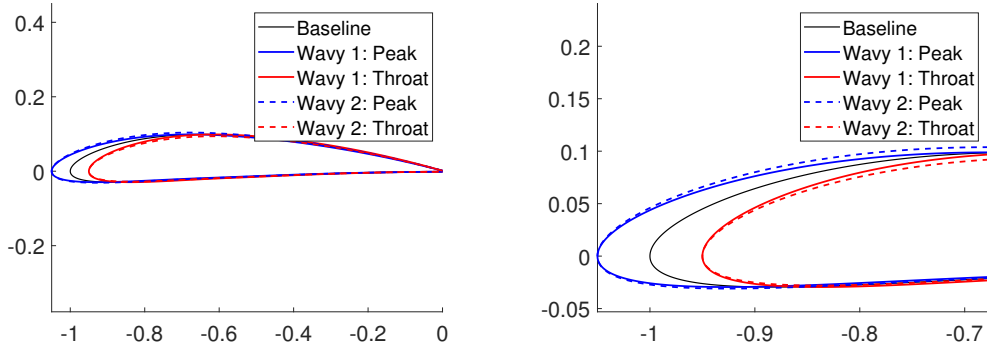
Figure 5.2: Cross-sections of Wavy 1 and Wavy 2 blades

In both configurations, the modification was implemented without changing the wetted surface area as the Baseline Propeller blade, allowing for a more direct comparison of performance between the modified and unmodified designs. Figure 5.3 shows the modified blades and the superimposition of the two designs, which highlights the differences in the humps and depressions along the suction side between the two configurations. In Wavy 2, where the thickness was scaled proportionally with the chord length, the humps are more pronounced, while in Wavy 1, the depressions are shallower.

5.2 Simulation set-up

The mesh generation and simulation setup for the propeller with leading edge tubercles were carried out in the same manner as for the Baseline Propeller, validated in Chapter 4. This allowed a direct comparison of results between the two modified designs and the reference propeller.

The computational domain was divided into a stationary region, with a diameter of $8D$ and length of $15D$, and a rotating region, with a diameter of $1.15D$ and length $0.4D$. The same mesh parameters and refinements were applied, and as a result, the final polyhedral meshes contained $11\,709\,216$ elements for Wavy 1 and $11\,552\,285$ for Wavy 2. The simulation setup, such as solver settings, turbulence and transition models, boundary conditions, and the steady-state approach (MRF), remained identical as for the Baseline Propeller, in order to ensure that any observed performance differences could be attributed to the presence of the tubercles rather than variations in the computational setup.
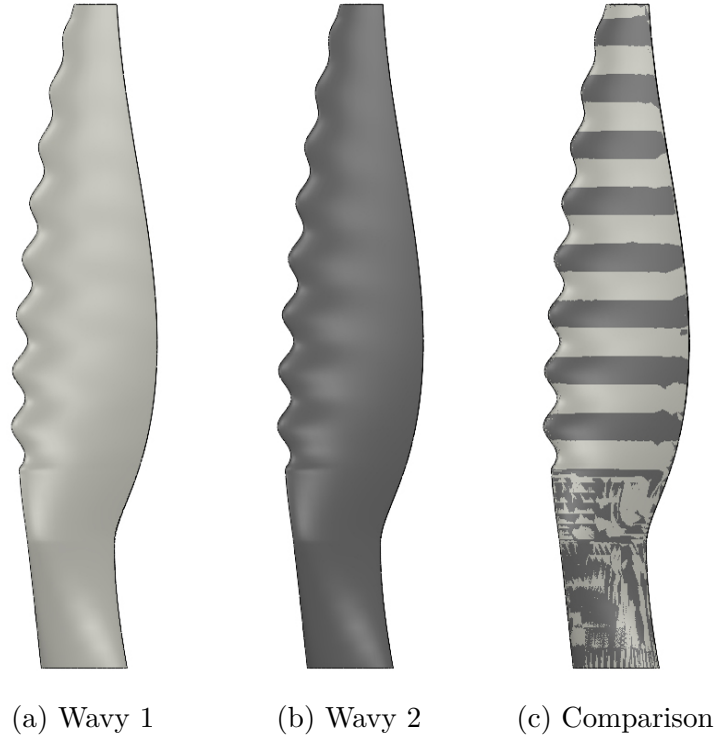
(a) Wavy 1   (b) Wavy 2   (c) Comparison

Figure 5.3: Designs of propeller blades with leading edge tubercles

5.3   Results

The simulations were performed to cover and compare all advance ratios analyzed for the Baseline Propeller. Table 5.1 presents C_T, C_Q, and η for Wavy 1 and Wavy 2, along with their relative differences from the values computed for the Baseline Propeller.

The analysis of Wavy 1 and Wavy 2 configurations revealed interesting trends with respect to the Baseline Propeller. They exhibited a reduction in C_T at all advance ratios, with the most significant drop observed at $J = 0.0025$, where Wavy 2 showed a decrease of 8.62% compared to the reference model. As the advance ratio increases, the performance gap between the modified propellers and the baseline narrows, particularly at $J = 0.6$, where the difference is less than 1% for both configurations. In terms of C_Q, both configurations showed a significant increase in hovering ($J = 0.0025$), with approximately a 6.5% rise compared to the Baseline Propeller. However, this effect becomes negligible as the advance ratio increases. The overall efficiency η follows a similar trend to the thrust coefficient, with both Wavy 1 and Wavy 2 underperforming the Baseline Propeller. At lower advance ratios, the efficiency decrease is more pronounced, while at intermediate advance ratios, such as from $J = 0.24$ to $J = 0.6$, the difference is less than 2%. The

Table 5.1: Comparison between Wavy 1, Wavy 2 and Baseline Propeller performance computed with the steady-state (MRF) method

Thrust Coefficient

J	Baseline	Wavy 1	Diff	Wavy 2	Diff
0.0025	0.1185	0.1087	-8.24%	0.1083	-8.62%
0.12	0.1094	0.1045	-4.49%	0.1048	-4.25%
0.24	0.0972	0.0949	-2.42%	0.0951	-2.18%
0.4	0.0734	0.0722	-1.59%	0.0724	-1.41%
0.6	0.0353	0.0351	-0.55%	0.0350	-0.69%
0.8	-0.0085	-0.0089	-5.43%	-0.0091	-7.18%

Torque Coefficient

J	Baseline	Wavy 1	Dist	Wavy 2	Dist
0.0025	0.0077	0.0082	6.48%	0.0082	6.56%
0.12	0.0080	0.0080	0.63%	0.0080	0.51%
0.24	0.0081	0.0080	-0.63%	0.0080	-0.64%
0.4	0.0073	0.0072	-0.68%	0.0072	-0.59%
0.6	0.0048	0.0048	0.02%	0.0048	-0.12%
0.8	~ 0	~ 0	$\sim 0\%$	~ 0	$\sim 0\%$

Efficiency

J	Baseline	Wavy 1	Dist	Wavy 2	Dist
0.0025	/	/	/	/	/
0.12	0.2613	0.2480	-5.09%	0.2490	-4.73%
0.24	0.4611	0.4528	-1.80%	0.4539	-1.54%
0.4	0.6418	0.6359	-0.91%	0.6365	-0.82%
0.6	0.7021	0.6980	0.58%	0.6980	-0.57%
0.8	-1.5850	-1.8490	-16.66%	-1.9277	-21.62%

verification and validation process indicated that for $J = 0.8$, CFD data were not reliable; for this reason, considerations for this advance ratio are not further discussed.

Figure 5.4 illustrates the surface streamlines of Wavy 1, Wavy 2, and the Baseline Propeller. The introduction of tubercles creates additional vorticity and complex flow patterns, which makes it difficult to clearly identify a laminar separation followed by a turbulent reattachment. Only flow separation can be recognized, and, following the same trend as the Baseline Propeller, the location of the separation on both Wavy configurations shifts toward the leading edge as the advance ratio decreases. As reported in [3, 9, 30], streamlines originating from the peaks appear to separate later than those from the throats. A reattachment line across the blade

span is not clearly visible, in contrast with the flow pattern of the Baseline Propeller, which might explain the reduction in C_T, particularly at lower advance ratios.

(a) $J = 0.0025$

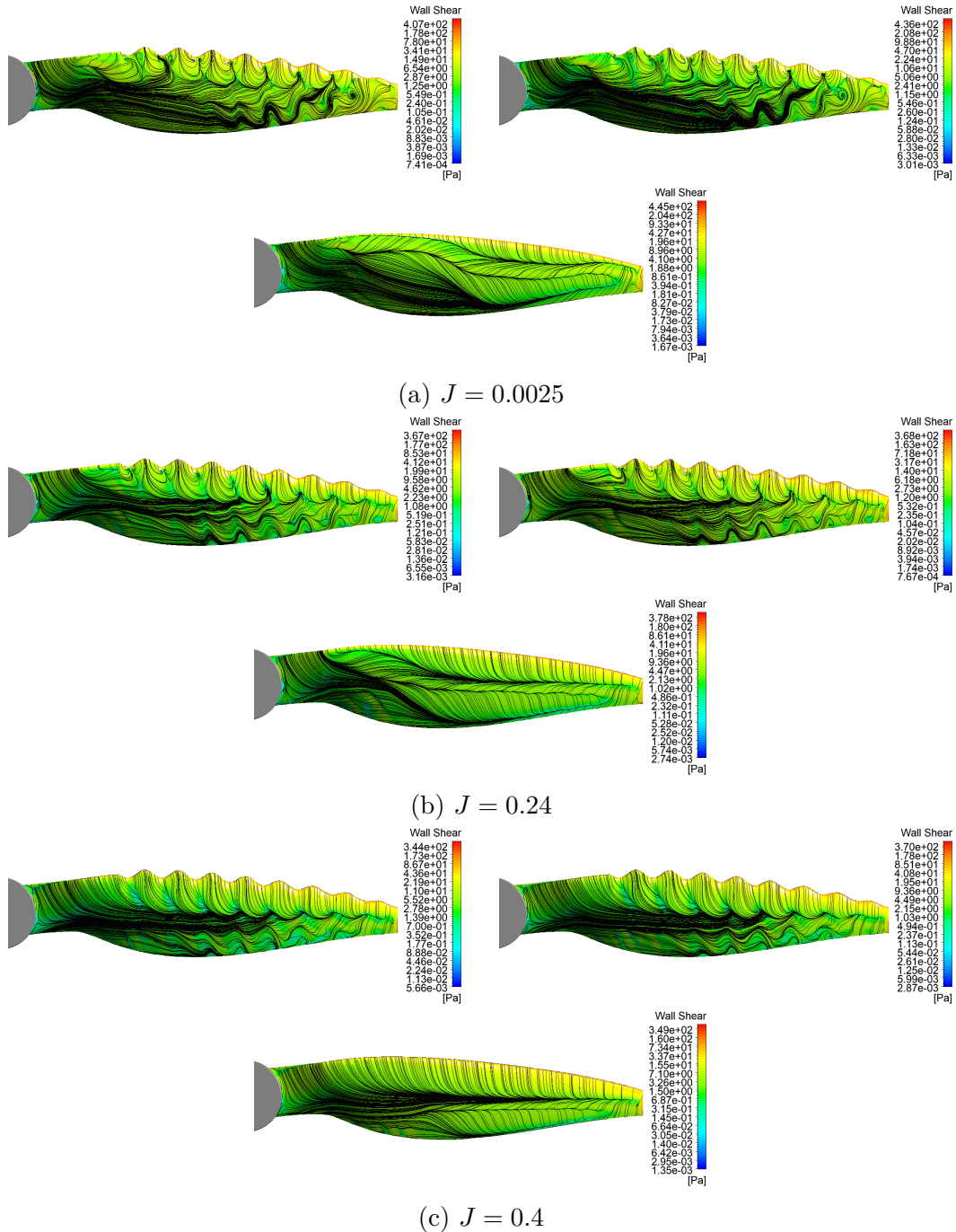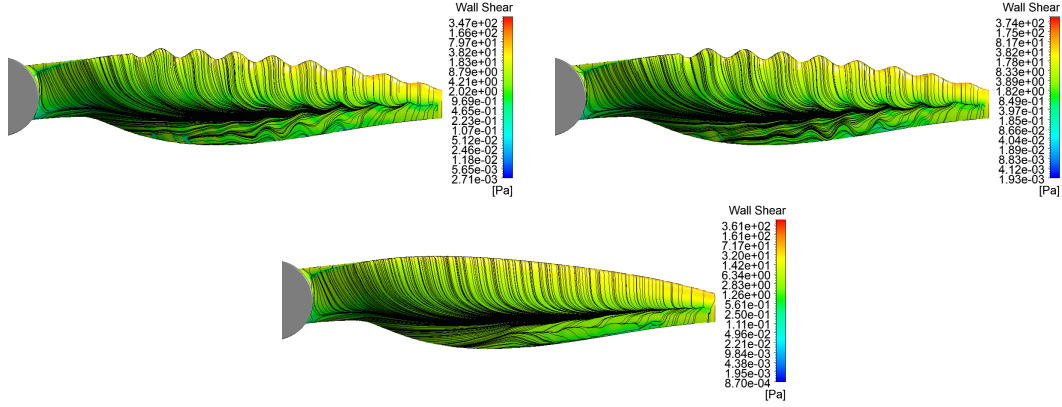
(b) $J = 0.24$

(c) $J = 0.4$

Figure 5.4: Surface streamlines on the blade suction side for Wavy 1 (top-left), Wavy 2 (top-right), and Baseline Propeller (bottom)

(d) $J = 0.6$

Figure 5.4: Surface streamlines on the blade suction side for Wavy 1 (top-left), Wavy 2 (top-right), and Baseline Propeller (bottom)

The pressure coefficient C_p and skin friction coefficient c_f plots (Figures 5.5 and 5.6) provided additional insights into the flow behavior around the modified blades. The most suitable cross-section for comparison is at $r/R = 0.6$, as it is sufficiently far from the hub and tip, and lies between a peak and a throat. This is also the region where the blade contributes most significantly to thrust. At this location, despite the pressure distribution does not show significant differences in absolute values at all advance ratios compared to the Baseline Propeller, a pressure plateau followed by a pressure rise is not clearly visible. However, changes in the chordwise skin friction coefficient on the suction side indicate that separation and reattachment might occur. At $J = 0.0025$, the flow appears to be separated, but at $r/R = 0.4$ and $r/R = 0.8$, turbulent reattachment might be present. This suggests that isolated regions of separation and reattachment could exist, even if they did not extend across the entire blade span, as for the Baseline Propeller. At $J = 0.24$ and $J = 0.4$, flow separation on the Wavy configurations occurs closer to the leading edge compared to the smooth blade. Additionally, turbulent separation might be present at approximately 80% of the chord length. Overall, Wavy 1 and Wavy 2 exhibited very similar flow behavior, but Wavy 1 showed larger regions with negative chordwise skin friction coefficients compared to Wavy 2, particularly at $r/R = 0.6$ at $J = 0.6$ and near the tip at $J = 0.0025$ and $J = 0.24$.

Figure 5.7 shows a comparison of C_p and c_f behind a peak and a throat. The chosen radial locations correspond to the peak and throat closer to $r/R = 0.6$, with the peak located at $r/R = 0.62$ and the throat at $r/R = 0.58$. This comparison highlights how the leading edge tubercles affect the flow around the blade, aligning with results found in the literature [3, 9, 30]. Wavy 1 and Wavy 2 produced similar

(a) $J = 0.0025$
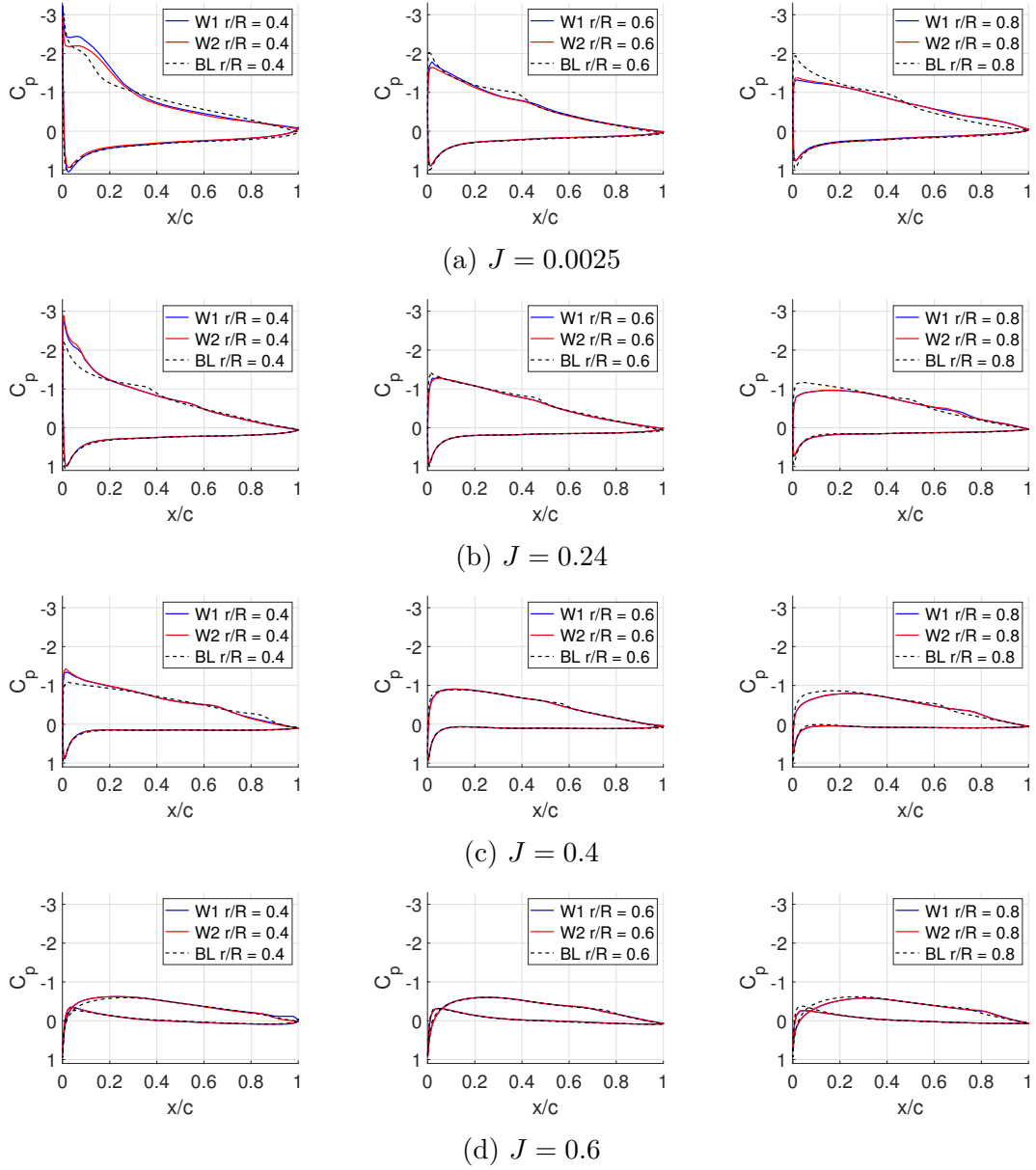
(b) $J = 0.24$

(c) $J = 0.4$

(d) $J = 0.6$

Figure 5.5: Pressure coefficient for Wavy 1, Wavy 2 and Baseline Propeller

results, both revealing that the flow originating from the throat separates earlier than the flow from the peak. This is easily visible in the skin friction coefficient plots: at $J = 0.0025$, the flow from the throat is fully detached, while the flow from the peak experiences a separation at approximately 40% of the chord, followed by a reattachment at $x/c \sim 0.6$. At $J = 0.24$ and $J = 0.4$, the flow from the throat separates at approximately 35% and 40% of the chord respectively, while the flow from the peak showed the same behavior as before, although the position of the

(a) $J = 0.0025$
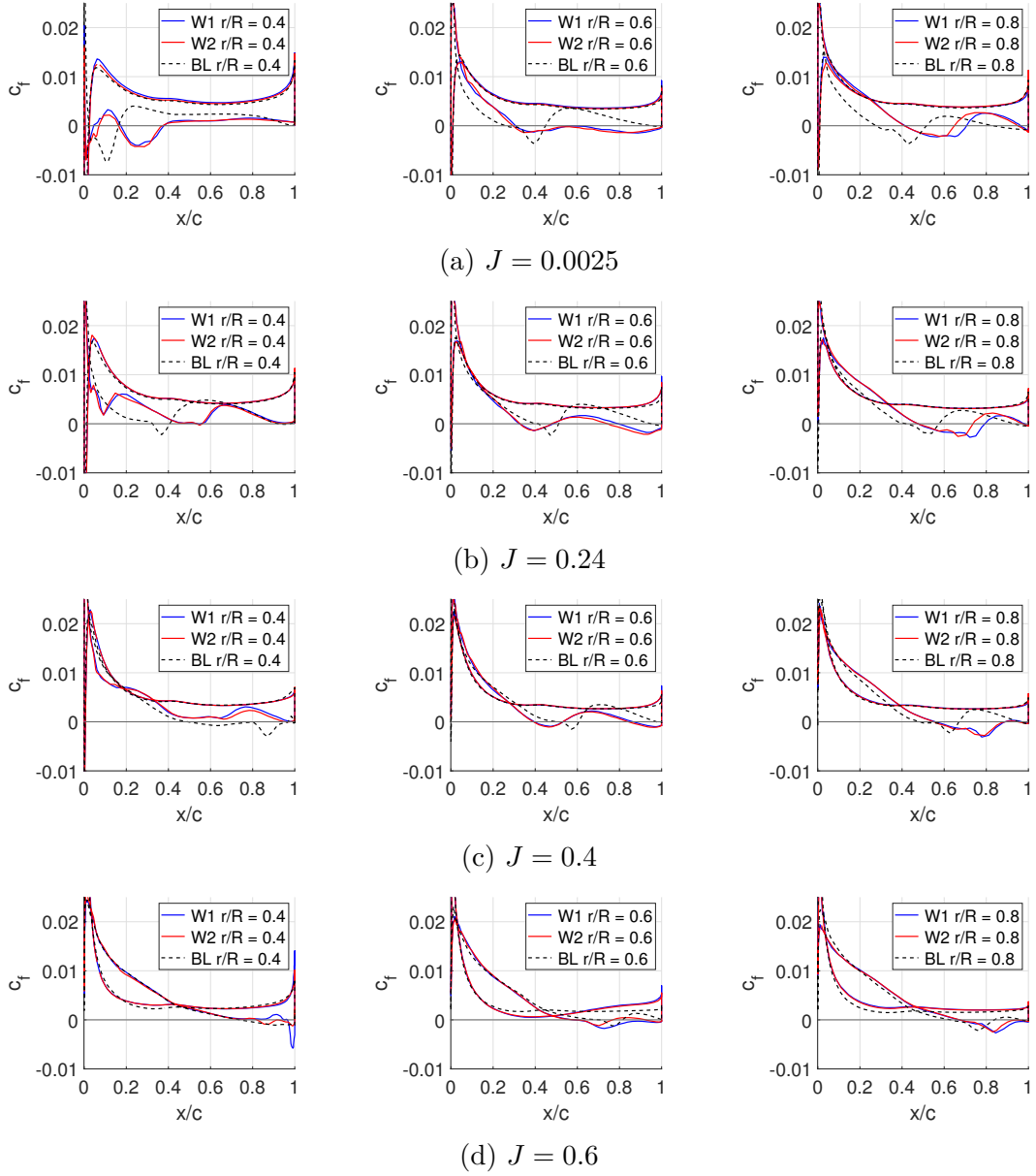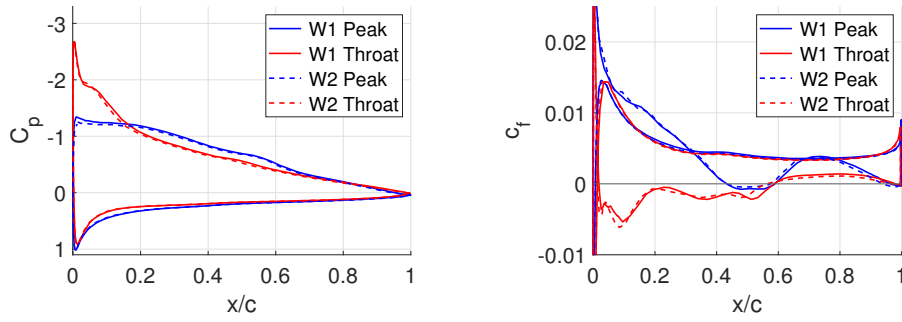
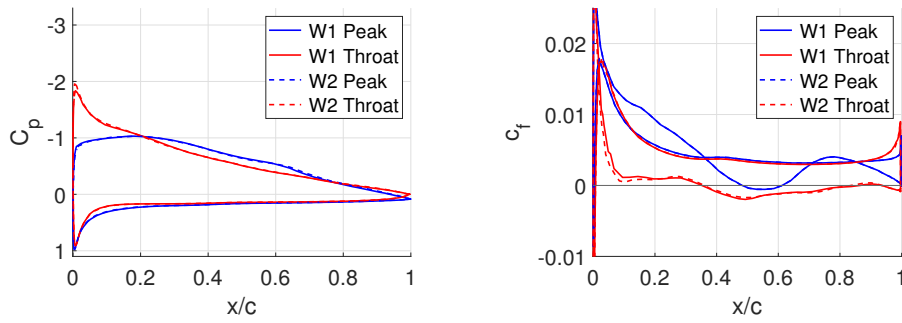(b) $J = 0.24$

(c) $J = 0.4$

(d) $J = 0.6$

Figure 5.6: Skin friction coefficient for Wavy 1, Wavy 2 and Baseline Propeller

separation bubble shifted downstream as the advance ratio increased. At $J = 0.6$, the flow from the peak appears to remain attached, while the flow from the throat separates at approximately 70%.
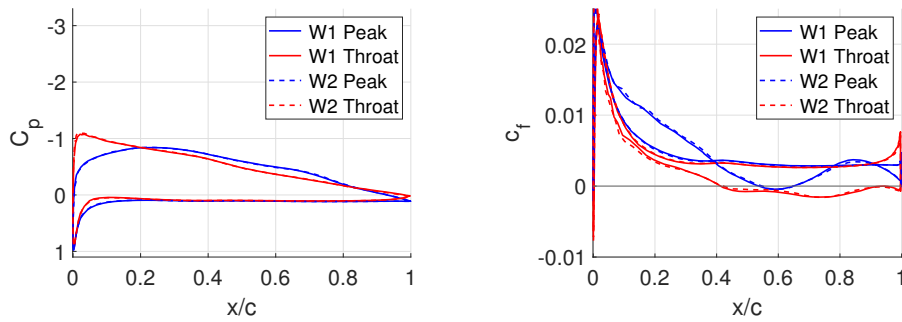
Figure 5.8 shows the vorticity along Y-axes, which runs from the leading edge toward the trailing. As reported [7, 13, 14, 30], tubercles appear to generate counter-rotating vortices between adjacent tubercles, energizing the boundary layer.
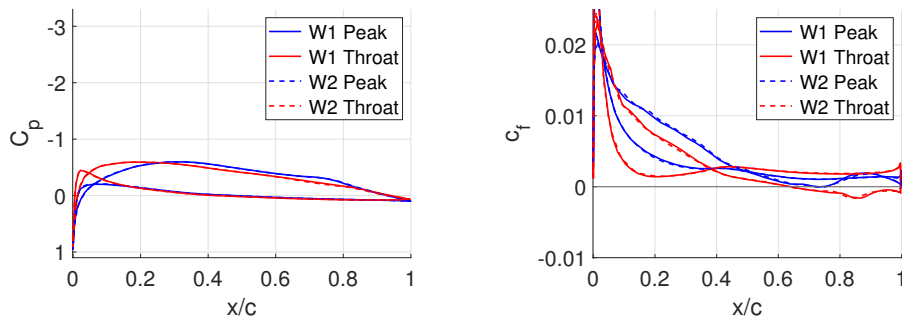
(a) $J = 0.0025$

(b) $J = 0.24$

(c) $J = 0.4$

(d) $J = 0.6$

Figure 5.7: Pressure and skin friction coefficients for a peak and a throat
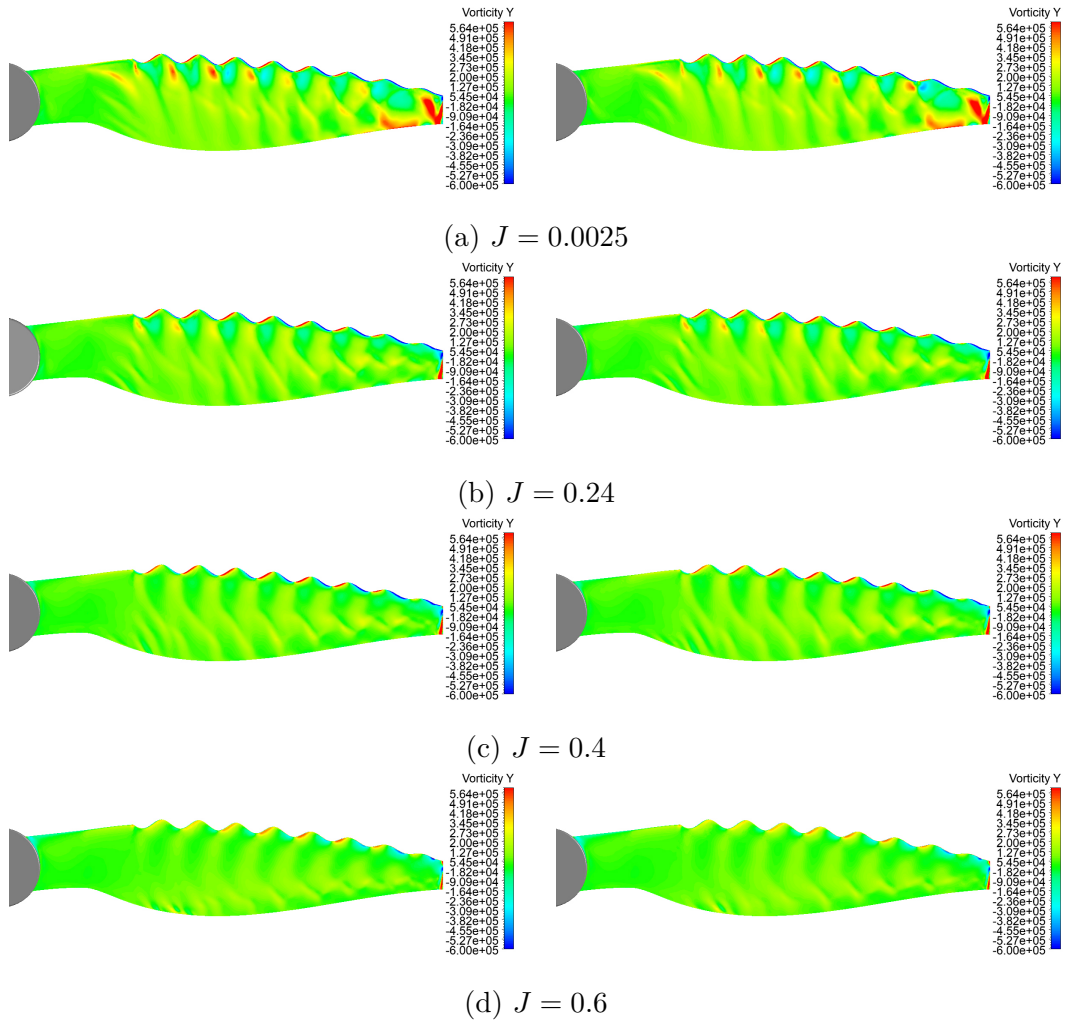
(a) $J = 0.0025$

(b) $J = 0.24$

(c) $J = 0.4$

(d) $J = 0.6$

Figure 5.8: Y vorticity

Chapter 6

Conclusions

The goal of this thesis was to evaluate the effects of leading edge tubercles on the aerodynamic performance of a drone propeller designed to operate at low Reynolds numbers. This bio-inspired modification comes from the flippers of Humpback Whales, where protuberances have shown potential as a passive flow control device. In the study, tubercles have been analyzed to understand their impact on thrust, torque and efficiency of the propeller and on the Laminar Separation Bubble that forms on the suction side of the blades.

A detailed numerical study was conducted using ANSYS Fluent. The simulation set-up was validated by comparing the computational results of the Baseline Propeller with experimental data. The verification and validation process demonstrated that the SST $k-\omega$ Turbulence Model, coupled with the γ-Algebraic Transition Model, was suitable for predicting the performance coefficients of the propeller using the steady-state Multiple Reference Frame approach on a mesh of approximately 11 million cells with a $y^+ < 1$. Results indicated that the Thrust Coefficient was overestimated at lower advance ratios, from $J = 0.0025$ to $J = 0.24$, and underestimated at higher advance ratios, but relative errors never exceeded 10% up to $J = 0.6$. The Torque Coefficient showed good agreement with experimental data, with relative errors consistently below 4.5% up to $J = 0.6$. However, the numerical simulations provided slightly larger errors in hovering and struggled to predict propeller performance at $J = 0.8$, where reverse thrust occurred. Additionally, the numerical model predicted the presence of a Laminar Separation Bubble on the suction side of the Baseline Propeller's blades, according with the oil-flow visualization, particularly at higher advance ratios. However, the location of the turbulent reattachment was consistently underestimated.

Leading edge tubercles changed the flow characteristics. The additional vorticity introduced by the modified leading edge led to complex flow patterns, which made it difficult to clearly identify a laminar separation followed by a turbulent

reattachment. In terms of aerodynamic performance, both Wavy configurations exhibited a reduction in C_T at all advance ratios, with the most significant drop observed in hovering, where Wavy 2 showed a decrease of 8.62% compared to the Baseline Propeller. However, the gap narrowed as the advance ratio increased, up to less than 1% at $J = 0.6$. The effect on the Torque coefficient was negligible for advance ratios ranging from $J = 0.12$ to $J = 0.6$, while a relative error of approximately 6.5% was computed at $J = 0.0025$. This performance degradation aligns with results in the literature, which indicate that tubercles improve post-stall behavior but reduce the maximum lift coefficient and slightly increase drag before stall at low Reynolds numbers. Thanks to surface streamlines, as well as pressure and skin friction coefficient plots, it was demonstrated that the Wavy designs did not exhibit a clear pattern like the Baseline Propeller, which was characterized by a laminar separation followed by a turbulent reattachment. Only flow separation could be clearly observed, with a separation point that moves toward the leading edge as the advance ratio decreases. Consistent with findings from the literature, it was observed that streamlines originating from the peaks separated later than those from the throats, though no clear reattachment line was identified across the blade span. Nonetheless, skin friction coefficient plots suggested the presence of isolated regions of separation and reattachment behind the peaks.

6.1   Future work

Future research could extend these results in several areas.

- **Optimization of tubercles geometry.** The values of amplitude and wavelength used to design the tubercles leading edge modification were chosen to balance the effects analyzed in the literature. However, an optimization of this geometry could lead to different results. Future work should focus on varying tubercle dimensions to identify whether an optimal configuration exists. Additionally, different design methodologies from the two adopted for this thesis might be explored.

- **Aeroacoustic performance.** The Baseline Propeller was extensively studied from an aeroacoustic point of view, revealing that the Laminar Separation Bubble on the suction side of the blades causes vortex shedding that leads to high-frequency broadband noise. Analyzing the effect of leading edge tubercles on the aeroacoustic behavior would be interesting, considering that the Wavy configurations did not exhibit a clear LSB.

- **Experimental Validation.** Wind tunnel tests of the Wavy propellers would provide a direct comparison with the computational data. This validation is essential to confirm the predicted effects of tubercles on thrust, torque and efficiency.

Bibliography

[1] IH Ibrahim and TH New. Tubercle modifications in marine propeller blades. pages 1–11, 2015.

[2] KL Hansen, RM Kelso, and BB Dally. An investigation of three-dimensional effects on the performance of tubercles at low reynolds numbers. In *17th Australasian Fluid Mechanics Conference, Auckland, New Zealand*, pages 5–9, 2010.

[3] Hamid Johari, Charles Henoch, Derrick Custodio, and Alexandra Levshin. Effects of leading-edge protuberances on airfoil performance. *AIAA journal*, 45(11):2634–2642, 2007.

[4] Edoardo Grande, Gianluca Romani, Daniele Ragni, Francesco Avallone, and Damiano Casalino. Aeroacoustic investigation of a propeller operating at low reynolds numbers. *AIAA Journal*, 60(2):860–871, 2022.

[5] Renato Tognaccini. *Lezioni di Aerodinamica dell'ala rotante*.

[6] Justin Winslow, Hikaru Otsuka, Bharath Govindarajan, and Inderjit Chopra. Basic understanding of airfoil characteristics at low reynolds numbers (10 4–10 5). *Journal of aircraft*, 55(3):1050–1061, 2018.

[7] Franke E Fish and Juliann M Battle. Hydrodynamic design of the humpback whale flipper. *Journal of morphology*, 225(1):51–60, 1995.

[8] DS Miklosovic, MM Murray, LE Howle, and FE Fish. Leading-edge tubercles delay stall on humpback whale (megaptera novaeangliae) flippers. *Physics of fluids*, 16(5):L39–L42, 2004.

[9] Paul W Weber, Laurens E Howle, Mark M Murray, and David S Miklosovic. Computational evaluation of the performance of lifting surfaces with leading-edge protuberances. *Journal of Aircraft*, 48(2):591–600, 2011.

[10] Hugo Carreira Pedro and Marcelo Kobayashi. Numerical study of stall delay on humpback whale flippers. page 584, 2008.

[11] Nikan Rostamzadeh, Kristy Hansen, and Richard Kelso. Tubercled wing flow physics and performance. *Flow Control Through Bio-inspired Leading-Edge Tubercles: Morphology, Aerodynamics, Hydrodynamics and Applications*, pages 41–68, 2020.

[12] Kristy L Hansen, Richard M Kelso, and Bassam B Dally. Performance variations of leading-edge tubercles for distinct airfoil profiles. *AIAA journal*, 49(1):185–194, 2011.

[13] Callum Stark, Weichao Shi, and Moritz Troll. Cavitation funnel effect: Bioinspired leading-edge tubercle application on ducted marine propeller blades. *Applied Ocean Research*, 116:102864, 2021.

[14] Fahad Rafi Butt and Tariq Talha. Numerical investigation of the effect of leading-edge tubercles on propeller performance. *Journal of Aircraft*, 56(3):1014–1028, 2019.

[15] Michael Jordan Stanway. *Hydrodynamic effects of leading-edge tubercles on control surfaces and in flapping foil propulsion.* PhD thesis, Massachusetts Institute of Technology, 2008.

[16] Fred Ernest Weick. *Aircraft propeller design.* McGraw-Hill Book Company, Incorporated, 1930.

[17] H. 1892-1934 Glauert. *The elements of aerofoil and airscrew theory.* The University press; 1943, England, 1943.

[18] DC Wilcox. *Turbulence Modeling for CFD.* 1998.

[19] Philippe Spalart and Steven Allmaras. A one-equation turbulence model for aerodynamic flows. page 439, 1992.

[20] Manuel Carreno Ruiz. Cfd simulation of propellers: Best practices analysis.

[21] Andrea Manavella. Validazione delle prestazioni di eliche a bassi numeri di reynolds tramite analisi cfd e modelli di ordine ridotto, 2021.

[22] Florian R Menter. Two-equation eddy-viscosity turbulence models for engineering applications. *AIAA journal*, 32(8):1598–1605, 1994.

[23] Weeratunge Malalasekera. *An introduction to computational fluid dynamics: the finite volume method.* Pearson Prentice Hall, 2007.

[24] Robin B Langtry and Florian R Menter. Correlation-based transition modeling for unstructured parallelized computational fluid dynamics codes. *AIAA journal*, 47(12):2894–2906, 2009.

[25] Florian R Menter, R Langtry, and Stefan Völker. Transition modelling for general purpose cfd codes. *Flow, turbulence and combustion*, 77:277–303, 2006.

[26] ANSYS Fluent. Ansys fluent theory guide. *Ansys Inc., USA*.

[27] Damiano Casalino, Gianluca Romani, Raoyang Zhang, and Hudong Chen. Lattice-boltzmann calculations of rotor aeroacoustics in transitional boundary layer regime. *Aerospace Science and Technology*, 130:107953, 2022.

[28] Damiano Casalino, Edoardo Grande, Gianluca Romani, Daniele Ragni, and Francesco Avallone. Definition of a benchmark for low reynolds number propeller aeroacoustics. *Aerospace Science and Technology*, 113:106707, 2021.

[29] Edoardo Grande, Daniele Ragni, Francesco Avallone, and Damiano Casalino. Laminar separation bubble noise on a propeller operating at low reynolds numbers. *AIAA Journal*, 60(9):5324–5335, 2022.

[30] Derrick Custodio. The effect of humpback whale-like leading edge protuberances on hydrofoil performance. *Worcester Polytechnic Institute*, 75, 2007.